Article

Spin transport in a tunable Heisenberg model realized with ultracold atoms

https://doi.org/10.1038/s41586-020-3033-y

Received: 18 May 2020

Accepted: 25 September 2020

Published online: 16 December 2020

Check for updates

Paul Niklas Jepsen[1,2,3]✉, Jesse Amato-Grill[1,2,3], Ivana Dimitrova[1,2,3], Wen Wei Ho[3,4], Eugene Demler[3,4] & Wolfgang Ketterle[1,2,3]

Simple models of interacting spins have an important role in physics. They capture the properties of many magnetic materials, but also extend to other systems, such as bosons and fermions in a lattice, gauge theories, high-temperature superconductors, quantum spin liquids, and systems with exotic particles such as anyons and Majorana fermions[1,2]. To study and compare these models, a versatile platform is needed. Realizing such systems has been a long-standing goal in the field of ultracold atoms. So far, spin transport has only been studied in systems with isotropic spin–spin interactions[3–12]. Here we realize the Heisenberg model describing spins on a lattice, with fully adjustable anisotropy of the nearest-neighbour spin–spin couplings (called the XXZ model). In this model we study spin transport far from equilibrium after quantum quenches from imprinted spin-helix patterns. When spins are coupled only along two of three possible orientations (the XX model), we find ballistic behaviour of spin dynamics, whereas for isotropic interactions (the XXX model), we find diffusive behaviour. More generally, for positive anisotropies, the dynamics ranges from anomalous superdiffusion to subdiffusion, whereas for negative anisotropies, we observe a crossover in the time domain from ballistic to diffusive transport. This behaviour is in contrast with expectations from the linear-response regime and raises new questions in understanding quantum many-body dynamics far away from equilibrium.

Quantum dynamics is an active research area in many-body physics. Even the linear-response (near-equilibrium) behaviour of many-body systems can be very complex. For example, spin transport in one-dimensional Heisenberg XXZ quantum spin chains, despite being a topic that is decades old, is still under active investigation because of the rich dynamics connected to integrability[13–17]. Dynamics in highly out-of-equilibrium scenarios, such as from continual drives or quantum quenches[18–22], is even less well understood. It is hence highly desirable to have a quantum simulator that can realize well isolated, programmable and controllable spin systems. By now, a number of such platforms exist[21–27], with varying capabilities.

Ultracold atoms in optical lattices offer an especially promising platform with which to realize tunable Heisenberg spin models[27]: in deep lattices where atoms become localized on individual sites, forming a Mott insulator[28], the dynamics of the remaining degrees of freedom is governed by effective spin–spin interactions realizing nearest-neighbour Heisenberg XXZ spin models. For bosons, the most commonly used atom, ^{87}Rb, has almost equal singlet and triplet scattering lengths, implying effectively isotropic spin physics[4–7]. For fermions, the Pauli exclusion principle enforces isotropic antiferromagnetism[3]. Many theoretical proposals have suggested ways to obtain richer spin models in optical lattices[29–32] over the past 20 years, and we now report here the realization of the spin-1/2 Heisenberg model with fully adjustable anisotropy in the spin–spin interactions. This enables simulations of anisotropic magnetic materials with easy-axis or easy-plane alignment. The wide tunability is realized using ^{7}Li atoms, the Feshbach resonances of which we have characterized in previous work[33]. Additionally, lithium, with its light mass, has the advantage of fast spin dynamics (set by second-order tunnelling)[26], decreasing the relative importance of heating and loss processes compared to heavier atoms. We use this fast and tunable platform to study far-from-equilibrium spin transport in previously unexplored regimes.

For many-body quantum simulation experiments, an ideal starting point is a simple benchmark system to which more complexity can be added. In this work, we first implement the XX model in one dimension, which is exactly solvable by mapping to a system of non-interacting fermions. We then tune the anisotropy to arbitrary values, which in the fermionic language corresponds to adding nearest-neighbour interactions. To implement the spin model, we use a system of two-component bosons in an optical lattice, which is well described by the Bose–Hubbard model. The two states, labelled $|\uparrow\rangle$ and $|\downarrow\rangle$, form a spin-1/2 system. In the Mott insulating regime at unity filling the effective Hamiltonian is given by the spin-1/2 Heisenberg XXZ model[29–32]

$$H = \sum_{\langle ij \rangle} \left[J_{xy} \left(S_i^x S_j^x + S_i^y S_j^y \right) + J_z S_i^z S_j^z \right], \quad (1)$$

where nearest-neighbour $\langle ij \rangle$ couplings are mediated by superexchange. To leading order, $J_{xy} = -4\tilde{t}^2/U_{\uparrow\downarrow}$ and $J_z = 4\tilde{t}^2/U_{\uparrow\downarrow} - (4\tilde{t}^2/U_{\uparrow\uparrow} + 4\tilde{t}^2/U_{\downarrow\downarrow})$, where $\tilde{t}$ is the tunnelling matrix element between neighbouring sites,

[1]Department of Physics, Massachusetts Institute of Technology, Cambridge, MA, USA. [2]Research Laboratory of Electronics, Massachusetts Institute of Technology, Cambridge, MA, USA. [3]MIT-Harvard Center for Ultracold Atoms, Cambridge, MA, USA. [4]Department of Physics, Harvard University, Cambridge, MA, USA. ✉e-mail: jepsen@mit.edu

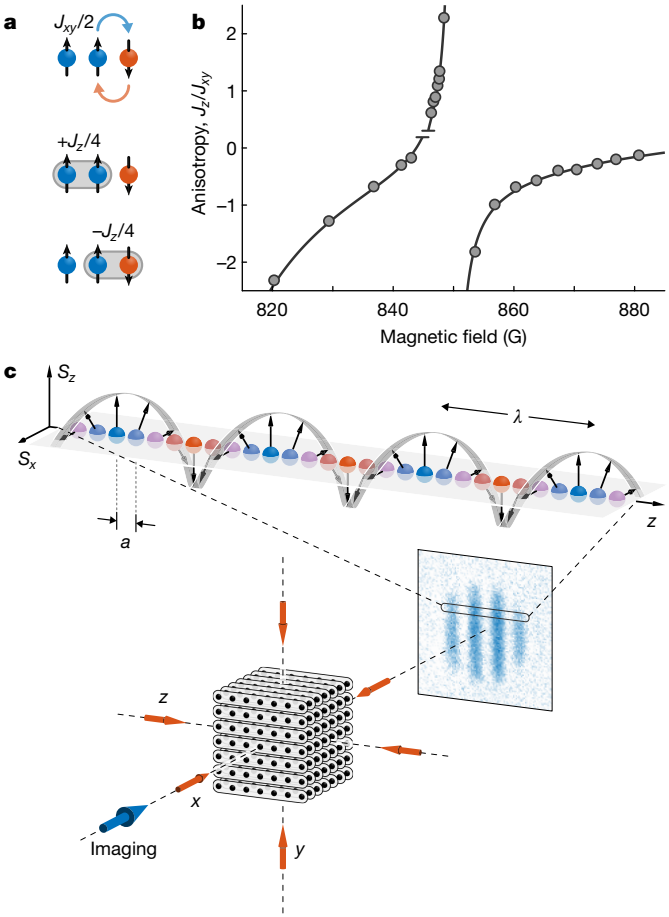

Fig. 1 | Tunability of the XXZ model with ^{7}Li and implemenation of a spin helix. a, The Hamiltonian (equation (1)) is characterized by two energy scales: the transverse spin coupling J_{xy} (spin exchange) and the longitudinal spin coupling J_z (spin–spin interaction). **b**, Anisotropy $\Delta = J_z/J_{xy}$ as a function of applied magnetic field. The solid line is a fit to experimental data points, which are calculated from measured values $U_{\uparrow\uparrow}$, $U_{\uparrow\downarrow}$, $U_{\downarrow\downarrow}$ (see Methods and Extended Data Fig. 1). **c**, Spin helix realized from two hyperfine states (spin $|\uparrow\rangle$ and $|\downarrow\rangle$). The spin vector winds in the S_z–S_x plane as a function of position z in the spin chain. Deep optical lattices along x and y create an array of independent spin chains. The z lattice is shallower and controls spin transport along each chain.

and $U_{\uparrow\uparrow}$, $U_{\uparrow\downarrow}$, $U_{\downarrow\downarrow}$ are the on-site interaction energies. The transverse coupling J_{xy} induces spin exchange between neighbouring sites and is the origin of spin transport. The longitudinal coupling J_z corresponds to a nearest-neighbour spin–spin interaction (Fig. 1a).

The magnitude of superexchange can be varied over two orders of magnitude by changing the lattice depth, which scales the entire Hamiltonian. We control the anisotropy $\Delta = J_z/J_{xy}$ via an applied magnetic field that tunes the interactions through Feshbach resonances in two hyperfine states (Fig. 1b) while keeping $J_{xy} > 0$ (antiferromagnetic). The ability to tune the anisotropy over a wide range of positive and negative values allows us to explore dynamics beyond previous experiments[3–7] in which $\Delta \approx 1$.

An array of one-dimensional (1D) chains is implemented by a deep optical lattice (of depth V_x, $V_y = 35E_R$) in the x and y directions. The lattice depth V_z along the z direction controls the superexchange rate within the chains (Fig. 1c). Here $E_R = \pi^2\hbar^2/(2ma^2)$ denotes the recoil energy, where a is the lattice spacing, m the atomic mass and $\hbar$ the reduced Planck constant. After preparing an identical spin helix[7–9] with wavelength λ in each chain (see Methods), time evolution is initiated by rapidly lowering V_z. The dynamics following this quench is governed by the 1D XXZ model (equation (1)) with an anisotropy Δ selected by an appropriate applied magnetic field. After an evolution time t of up to $500\hbar/J_{xy}$ (well below the heating lifetime, approximately 1 s, of the Mott insulator), the dynamics is frozen by rapidly increasing V_z and the atoms are imaged in the $|\uparrow\rangle$ state via state-selective polarization-rotation imaging with an optical resolution of about 6 lattice sites (see Methods).

Integrating the images along the direction perpendicular to the chains yields a 1D spatial profile of the population in the $|\uparrow\rangle$ state, averaged over all spin chains (see Extended Data Fig. 2). This is equivalent to a measurement of the local magnetization $\langle S_i^z\rangle = (n_{i\uparrow} - n_{i\downarrow})/2 = n_{i\uparrow} - 1/2$ which, as in Fig. 1c, shows a sinusoidal stripe pattern. We determine the contrast $\mathcal{C}$ by a fit $f(z) = g(z)[1 + \mathcal{C}\cos(Qz + \theta)]/2$, where $Q = 2\pi/\lambda$ is the wavevector, $g(z)$ is a Gaussian envelope function that accounts for the spatial distribution of all atoms $n = n_\uparrow + n_\downarrow$, and θ is a random phase that varies from shot to shot, owing to small magnetic bias field drifts. During the evolution time t the contrast $\mathcal{C}(t)$ decays, and we study the dependence of $c(t) = \mathcal{C}(t)/\mathcal{C}(0)$ on lattice depth V_z, wavelength λ, and anisotropy Δ.

For all data, we measure spin dynamics at two or three different lattice depths V_z and verify that the decay curves $c(t)$ collapse when time is rescaled by the spin-exchange time $\hbar/J_{xy}$ (see for example, Fig. 2a). This demonstrates that we observe transport by superexchange and not some other process. To study transport behaviour, we measure how the decay timescale τ depends on the modulation lengthscale λ. We note that for ballistic motion, this decay constant grows linearly with distance ($\tau \propto \lambda$), whereas for diffusion it grows quadratically ($\tau \propto \lambda^2$). Throughout this Article, we normalize time by the spin-exchange time $\hbar/J_{xy}$, length by the lattice spacing a, and velocities by the Fermi velocity $v_F = a/(\hbar/J_{xy})$. These units are obtained from the experimentally determined lattice depth using an extended Hubbard model and have an estimated systematic calibration error of about ±10%, in addition to quoted statistical errors. The accuracy of Δ is estimated to be ±0.1 (see Methods). Unless noted otherwise, all error bars and uncertainties herein are purely statistical and represent 1σ uncertainty of the fits. Each data point for the contrast $c(t)$ is obtained by simultaneously fitting several images (usually six, but up to 15).

XX model

We first study the case $\Delta = 0$, which can be mapped by the Jordan–Wigner transformation[34] to non-interacting spinless fermions undergoing nearest-neighbour hopping on a lattice. In this mapping, $|\uparrow\rangle$ corresponds to a site occupied by a fermion, and $|\downarrow\rangle$ to an empty site. Small excitations around the Fermi sea at half-filling are spin waves with wavevector q and a linear dispersion relation $\omega(q) = v_F q$.

Figure 2a shows the decay of the contrast $c(t)$ for $\Delta \approx 0$ (see Methods for calibration of Δ). In addition to an overall decay, a local maximum corresponding to a partial revival of the initial spin modulation appears after about 12 spin-exchange times. We find the decay curves can be well described by the sum of a decaying part with time constant τ and a (damped) oscillating part with frequency ω, resulting in a fitting function $c(t) = [a_0 + b_0\cos(\omega t)]e^{-t/\tau} + c_0$, with a_0, b_0, c_0, ω and τ as adjustable parameters (Methods and Extended Data Fig. 4 discuss the offset c_0). Numerical simulations, also shown in Fig. 2a, reproduce the major features of the experimental dynamics very well (decay time τ and first oscillation), but differ in details, probably owing to a difference in hole fraction, uncertainties in Δ, or non-idealized initial-state preparation. By varying the wavelength $\lambda = 2\pi/Q$ of the helix (Fig. 2b) we obtain a dispersion relation $\omega(Q)$ for the oscillations (Fig. 2d). A linear fit $\omega(Q) = vQ$ yields a characteristic velocity $v = 0.76(1)v_F$, similar to the near equilibrium dynamics, as expected for a non-interacting system.

The decay time constant τ also shows a linear scaling with inverse wavevector: a power-law fit $\tau \propto Q^{-\alpha}$ yields an exponent of $\alpha = 1.00(5)$, indicating ballistic transport (Fig. 3b, red). Indeed, if we plot $c(t)$ in time units rescaled by λ, all curves for different helix wavelengths collapse into a single curve (Fig. 2c), showing that all aspects of the observed spin dynamics in the XX model are ballistic and governed by one characteristic velocity.

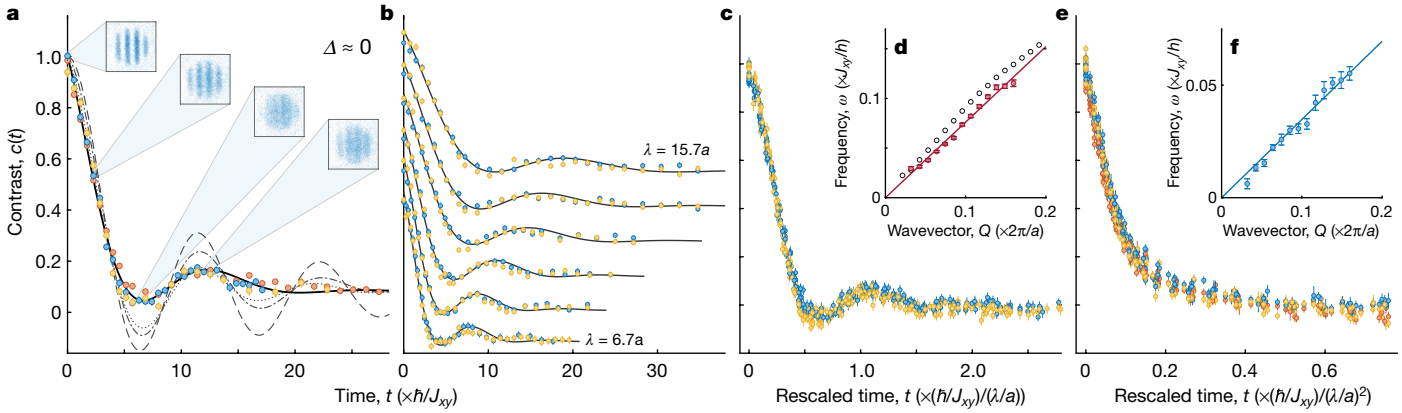

Fig. 2 | Ballistic and diffusive spin transport. a–d, XX model, ballistic behaviour ($\Delta \approx 0$, non-interacting fermions). **a**, Spin-helix contrast $c(t)$ for $\lambda = 10.4a$ measured at three different lattice depths $9E_R$ (orange), $11E_R$ (blue) and $13E_R$ (yellow). Decay curves collapse when times are expressed in units of $\hbar/J_{xy} = 0.64$ ms, 1.71 ms and 4.30 ms, respectively. The fit (black line) shows a decay with time constant $\tau = 5.5(2)\hbar/J_{xy}$ and a damped oscillation with period $T = 2\pi/\omega = 13.7(2)\hbar/J_{xy}$. The fit is typically applied to data points from all lattice depths simultaneously, but analysing each lattice depth separately yields identical results. Numerical simulations are also shown for the XX model (dashed line) and bosonic $\tilde{t}$–J model with 5% holes (dash-dotted line) and 10% holes (dotted line). **b**, Decay curves for different wavelengths $\lambda = 15.7a$, $13.4a$, $11.7a$, $9.4a$, $7.8a$ and $6.7a$ (offset for clarity). **c**, The decay curves in **b** collapse into a single curve, if time is rescaled by λ (indicating ballistic transport) and offsets c_0 are subtracted. **d**, Oscillation frequencies (filled symbols) follow a linear dispersion relation $\omega(Q) = vQ$ with velocity $v = 0.76(1)v_F$ and agree at the 10% level with numerical simulations (open symbols) yielding $v = 0.85(1)v_F$. Theoretical frequencies are obtained as the inverse of the first revival time. Owing to damping, this may be an overestimate of 10%. **e**, **f**, XXX model, diffusive behaviour ($\Delta \approx 1$, strongly interacting fermions). Oscillations are strongly suppressed and time has to be rescaled by λ^2 (indicating diffusive transport) for collapse. However this collapse is not perfect, because of the presence of small oscillations (see Extended Data Fig. 3) that follow a linear dispersion relation (**f**) with a velocity $v = 0.35(1)v_F$.

XXX model

For finite Δ, the Jordan–Wigner transformation results in fermions with nearest-neighbour interactions. The isotropic case $\Delta = 1$ corresponds to strong interactions, which should generically turn fast ballistic transport into slow diffusive transport. Indeed, the decay slows down for increasing wavelength λ much more dramatically than in the $\Delta \approx 0$ case (also illustrated in Extended Data Fig. 3a–c). A power-law fit of the decay constant τ versus Q yields an exponent of $\alpha = 1.87(4)$, which is close to 2, indicative of a diffusive process (Fig. 3b, blue). If time units are rescaled by λ^2, then all contrast curves $c(t)$ collapse very well into a single curve (Fig. 2e). However this collapse is not perfect, because of a (small) oscillating part that still obeys a linear dispersion relation $\omega(Q) = vQ$ (Fig. 2f).

Using $1/\tau = DQ^2$, a diffusion constant can be determined as $D = 0.242(7)a^2/(\hbar/J_{xy})$. Interpreting $D = \frac{1}{2}\delta x^2/\delta t$ as arising from a random walk of step size δx (the mean free path) and time δt between steps, and using $v = \delta x/\delta t = 0.35(1)v_F$ (obtained from the dispersion relation in Fig. 2f), we find $\delta x = 1.39(5)a$. A mean free path on the order of the lattice constant is analogous to the Mott–Ioffe–Regel limit for resistivity where simple quasi-particle pictures break down[35,36], implying that the isotropic Heisenberg model is strongly interacting.

Our observation of diffusive behaviour and the value for the diffusion coefficient are consistent with previous results[7] (for zero hole fraction) on the 1D isotropic Heisenberg model with $J_{xy} < 0$. Our system is antiferromagnetic ($J_{xy} > 0$), and so this indicates that the overall sign of the Hamiltonian is irrelevant, as expected from theoretical arguments involving time-reversal symmetry (see Methods). However the small (ballistic) oscillatory component has not been previously reported. We note that a two-dimensional Fermi–Hubbard system can also show diffusive decay and ballistic oscillations[37].

By tuning the interactions over a large range of Δ, we can study how the transport behaviour changes. For an interacting gas of classical particles or quasiparticles, one would expect ballistic behaviour on timescales shorter than the collision time and diffusion for longer times. We indeed find this for $\Delta < 0$, whereas for $\Delta \geq 0$ we observe qualitatively very different behaviour (also illustrated in Extended Data Fig. 5).

Positive anisotropies ($\Delta \geq 0$)

All measured decay curves $c(t)$ are well described by the fitting function previously used. The observed oscillation frequencies ω follow linear dispersion relations $\omega(Q) = vQ$ (Extended Data Fig. 3), whereas the decay time constants τ show power-law scaling $\tau \propto Q^{-\alpha}$ (Fig. 3) in the following way: as the anisotropy is increased from $\Delta = -0.12$ to $\Delta = 0.55$, the exponent stays close to $\alpha = 1$ ('ballistic regime') and the characteristic velocity of oscillations decreases by a factor of about 1.6, to $v = 0.47(1)v_F$. Between $\Delta \approx 0.5$ and 1 the exponent increases smoothly from $\alpha = 1$ to $\alpha \approx 2$ ('superdiffusive regime'), for example, $\alpha = 1.48(4)$ at $\Delta = 0.78$ (Fig. 3b, yellow). For $\Delta > 1$ transport slows down even more, and the exponent also continues to increase smoothly to values $\alpha > 2$ ('subdiffusive regime'), for example, $\alpha = 2.83(14)$ at $\Delta = 1.58$ (Fig. 3b, green). For each $\Delta \geq 0$, the measured decay curves collapse into a single curve, if time units are rescaled by λ^α (Extended Data Fig. 6).

Power-law exponents between 1 and 2 (superdiffusion) are often associated with Lévy flights or fractional Brownian motion where step sizes are correlated[38,39]. Power-law exponents larger than 2 (subdiffusion) typically arise for transport through a disordered medium[40,41] and have also been recently observed in a tilted Fermi–Hubbard system[42]. However, the XXZ Heisenberg Hamiltonian we study has no disorder.

Negative anisotropies ($\Delta < 0$)

Here the behaviour is qualitatively very different compared to positive Δ of similar magnitude. We find a crossover in the time domain from ballistic to diffusive behaviour. For example, at $\Delta = -1.43$ the initial decay of $c(t)$ is fast and, in fact, coincides well with the non-interacting (ballistic) case $\Delta \approx 0$ (Fig. 4a), in stark contrast to the positive case $\Delta = +1.58$ (Extended Data Fig. 5). At $t = t_0 \approx 2.8\hbar/J_{xy}$ (dotted line) the decay suddenly slows down. We therefore parameterize the decay curve $c(t)$ by a piecewise fit with two timescales: (I) a linear function $(1 - t/\tau_I)$ at short times and (II) an exponential $e^{-t/\tau_{II}}$ at longer times, with respective time constants τ_I, τ_{II}. When the wavevector Q is varied, both τ_I and τ_{II} follow a power law (Fig. 3a), but with different exponents: $\alpha_I = 1.08(6)$ (ballistic) and $\alpha_{II} = 2.15(16)$ (diffusive), respectively (Fig. 3c). In both experimental

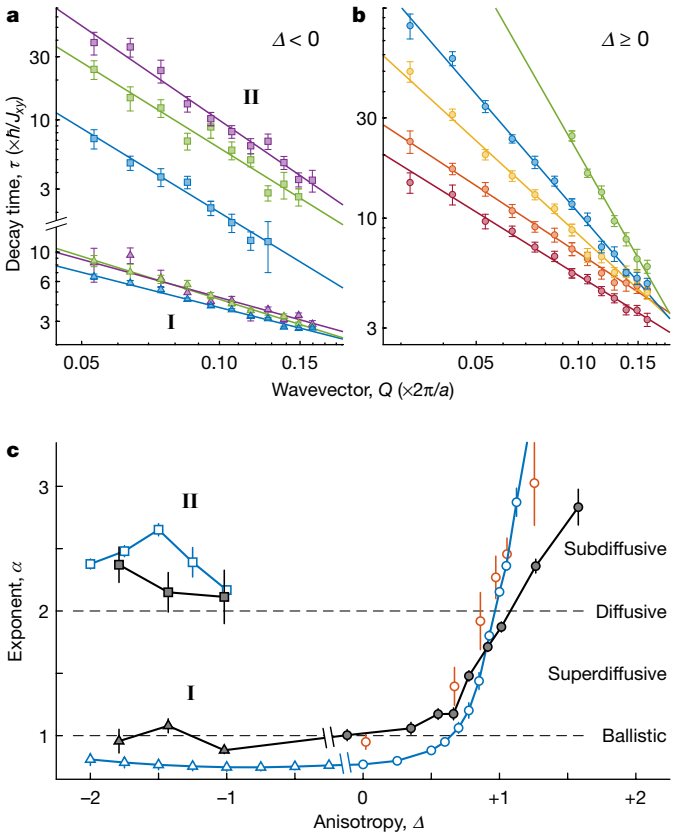

Fig. 3 | Power-law scalings. a, **b**, The power-law scalings of the decay time constants τ for anisotropies Δ ranging from negative (**a**) to positive (**b**). Experimental results are shown in **a** for $\Delta = -1.02$ (blue), −1.43 (green) and −1.79 (purple) for the two timescales τ_{I} and τ_{II}; and in **b** for $\Delta = -0.12$ (red), 0.35 (orange), 0.78 (yellow), 1.01 (blue) and 1.58 (green). Lines are power-law fits. **c**, Fitted power-law exponents from experiments (filled symbols) and theory (open symbols), obtained from simulations of the defect-free XXZ model (blue) and $\tilde{t}$–J model with 5% hole fraction (orange). **a**–**c** can be summarized as follows. For $\Delta \geq 0$ (circles), we observe anomalous diffusion: the exponent increases smoothly from ballistic (red and orange) to superdiffusive (yellow) to diffusive (blue) to subdiffusive (green). For $\Delta < 0$, we observe behaviour reminiscent of a classical gas: transport is ballistic at short times (I; triangles) and diffusive at longer times (II; squares). (For diffusion coefficients and theory see Extended Data Fig. 8.).

(Fig. 4b) and numerical results (Fig. 4c), all decay curves collapse for short times before 'peeling off' at later times, if time is rescaled by λ.

Similar behaviour is observed for other negative anisotropies (Fig. 3a; also Extended Data Fig. 7), with the initial ballistic temporal decay (regime I) almost independent of Δ. However, for larger $|\Delta|$, we find that t_0 (the range of regime I) is smaller, and the diffusion timescales τ_{II} in regime II are longer. The diffusion coefficient decreases from $D = 1.27(6)a^2/(\hbar/J_{xy})$ to $0.25(2)a^2/(\hbar/J_{xy})$ between $\Delta = -1.02$ and −1.79 (Extended Data Fig. 8c). Figure 3c summarizes the different transport behaviours uncovered for the anisotropic Heisenberg model and represents the main result of this paper.

Theoretical simulations

To validate our platform as a quantum simulator, we have carried out numerical simulations of quench dynamics starting from a spin helix, using a combination of exact diagonalization and tensor network methods (see Methods). We simulate the dynamics of the system without holes (XXZ Hamiltonian), as well as with a small probability of holes (bosonic $\tilde{t}$–J model), and compare the simulated contrast to experimental results. The timescales of decay generally agree fairly well. A qualitative difference in the decay curves is illustrated in Fig. 2a: the simulations always show an initial quadratic decay (as expected from time-reversal symmetry, see Methods), and revivals are generally more pronounced. The initial quadratic decay happens in the pure-spin simulations on the timescale of $\hbar/J_{xy}$, whereas an addition of 5% to 10% holes reduces this to the timescale $\hbar/\tilde{t}$ (where $\tilde{t}$ is the tunnelling amplitude in the $\tilde{t}$–J model)[7] and reduces the amplitude of revivals. However, the presence of holes does not affect the overall behaviour of the decay times of the spin contrast: the simulations of both the XXZ and the $\tilde{t}$–J model yield power-law scalings of time constants, with exponents that agree reasonably well with experimental ones (see Fig. 3c and Methods section 'Power-law scalings in the continuum limit').

Discussion

Our work on spin transport illustrates the strength of a combined experimental and theoretical quantum simulation. Our quantum simulator platform enables us to probe dynamical regimes that are difficult to achieve in numerical simulations, such as large system sizes or long times (Extended Data Figs. 6, 7), which require prohibitively large computational resources. On the other hand, numerical simulations provided valuable insight into effects that could not be studied experimentally, such as that of holes (Figs. 2a, 3c), different phases of the helix, and the role of boundary conditions (Extended Data Figs. 9, 10).

Our observations are consistent with some theoretical predictions for spin transport in the anisotropic Heisenberg model, but differ sharply from others. For example, studies of quantum quenches from pure states involving a single domain wall[43–46] have suggested ballistic dynamics at $\Delta = 0$ and diffusive dynamics at $\Delta = 1$ (albeit with logarithmic corrections), similar to our findings. In addition to diffusive transport, a ballistic light-cone has been observed[46] in numerics at $\Delta = 1$, which may be related to the small ballistic oscillatory component we have observed experimentally. In contrast to our findings, theoretical studies of long-time linear response of spin transport at high temperatures (that is, mixed states) have indicated a sharp transition from ballistic ($\Delta < 1$) to diffusive ($\Delta > 1$), with superdiffusive behaviour ($\alpha = 3/2$) exactly at the transition point $\Delta = 1$[15,16], which can be understood from generalized hydrodynamics involving local equilibriation of conserved quantities[47,48]. The situation we have studied is different, because the initial spin-helix state is a pure state far from equilibrium. An accurate description of coherent dynamics using the exact eigenstates from the Bethe ansatz[49] is a very challenging problem. Ultimately, the spin-helix state will relax into a thermal state (or quasi-thermal generalized Gibbs state), but probably outside the time window studied here. The rich phenomenology observed in our experiments and dramatic differences with the cases studied in the literature calls for a deeper understanding of this dynamical regime, both theoretically and experimentally.

Our studies can be extended in many different directions: the role of integrability, which the XXZ Hamiltonian possesses, should be explored, for example by adding next-nearest-neighbour integrability-breaking terms realized through appropriate Rydberg dressing of atoms. We can explore different initial conditions, including single domain walls[43–46] and finite temperatures (by using partially polarized (mixed) states) and study the decay of transverse spin via transport and dephasing. An interesting question is whether the power-law scalings change for very large wavelengths that approach the continuum limit (see preliminary theoretical analysis in Methods and Extended Data Fig. 8). We can furthermore realize Heisenberg models in two or three spatial dimensions, or with purely ferromagnetic couplings by changing the sign of J_{xy} using a constant force to tilt the lattice[50].

Online content

Any methods, additional references, Nature Research reporting summaries, source data, extended data, supplementary information, acknowledgements, peer review information; details of author contributions and competing interests; and statements of data and code availability are available at https://doi.org/10.1038/s41586-020-3033-y.

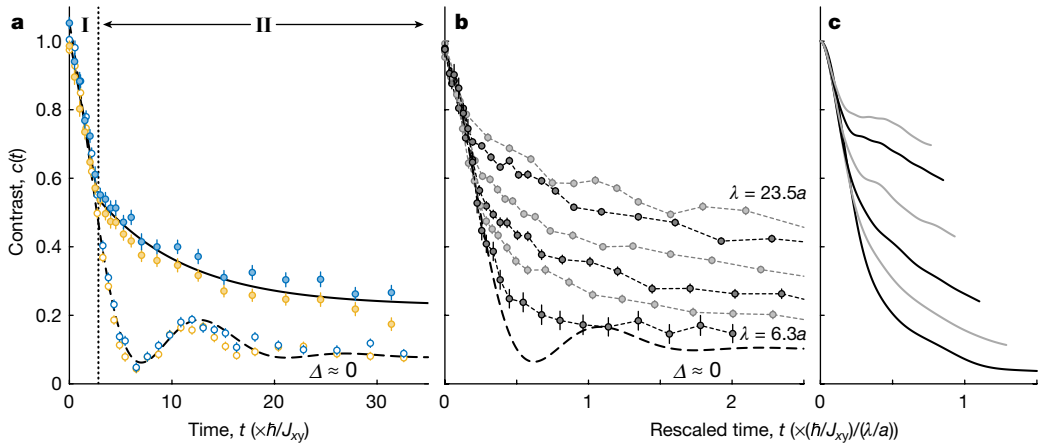

Fig. 4 | Temporal crossover from ballistic to diffusive transport for negative anisotropies $\Delta < 0$. a, Spin-helix contrast $c(t)$ for $\lambda = 10.4a$ and $\Delta = -1.43$ (filled circles) measured at lattice depths $11E_R$ (blue) and $13E_R$ (yellow). A piecewise fit (solid line) is linear at short times (I) and exponential at longer times (II) with a crossover at $t = t_0$ (vertical dotted line). For $t < t_0$ the decay coincides well with the non-interacting case $\Delta \approx 0$ (open circles and dashed line). **b**, Decay curves for different wavelengths $\lambda = 23.5a, 18.8a, 13.4a, 10.4a, 8.5a$ and $6.3a$ (average of measurements at lattice depths $11E_R$ and $13E_R$) collapse into a single curve at early times if time is rescaled by λ (as for ballistic behaviour) and follow the non-interacting case (thick dashed line). At later times, the decay is diffusive with different scaling (see Fig. 3a). **c**, Numerical simulations for $\Delta = -1.5$ and the same wavelengths λ as in **b** show similar behaviour, although the range of time probed is more limited. Simulations could not be extended to longer times, owing to the exponential increase in computation time.

1. Lee, P. A. From high temperature superconductivity to quantum spin liquid: progress in strong correlation physics. *Rep. Prog. Phys.* **71**, 012501 (2007).
2. Broholm, C. et al. Quantum spin liquids. *Science* **367**, eaay0668 (2020).
3. Nichols, M. A. et al. Spin transport in a Mott insulator of ultracold fermions. *Science* **363**, 383–387 (2019).
4. Brown, R. C. et al. Two-dimensional superexchange-mediated magnetization dynamics in an optical lattice. *Science* **348**, 540–544 (2015).
5. Fukuhara, T. et al. Quantum dynamics of a mobile spin impurity. *Nat. Phys.* **9**, 235–241 (2013).
6. Fukuhara, T. et al. Microscopic observation of magnon bound states and their dynamics. *Nature* **502**, 76–79 (2013).
7. Hild, S. et al. Far-from-equilibrium spin transport in Heisenberg quantum magnets. *Phys. Rev. Lett.* **113**, 147205 (2014).
8. Koschorreck, M., Pertot, D., Vogt, E. & Köhl, M. Universal spin dynamics in two-dimensional Fermi gases. *Nat. Phys.* **9**, 405–409 (2013); corrigendum **10**, 170 (2014).
9. Trotzky, S. et al. Observation of the Leggett–Rice effect in a unitary Fermi gas. *Phys. Rev. Lett.* **114**, 015301 (2015).
10. Palzer, S., Zipkes, C., Sias, C. & Köhl, M. Quantum transport through a Tonks–Girardeau gas. *Phys. Rev. Lett.* **103**, 150601 (2009).
11. Sommer, A., Ku, M., Roati, G. & Zwierlein, M. W. Universal spin transport in a strongly interacting Fermi gas. *Nature* **472**, 201–204 (2011).
12. Krinner, S. et al. Mapping out spin and particle conductances in a quantum point contact. *Proc. Natl. Acad. Sci. USA* **113**, 8144–8149 (2016).
13. Vasseur, R. & Moore, J. E. Nonequilibrium quantum dynamics and transport: from integrability to many-body localization. *J. Stat. Mech.* **2016**, 064010 (2016).
14. Bertini, B. et al. Finite-temperature transport in one-dimensional quantum lattice models. Preprint at https://arxiv.org/abs/2003.03334 (2020).
15. Ljubotina, M., Žnidarič, M. & Prosen, T. Spin diffusion from an inhomogeneous quench in an integrable system. *Nat. Commun.* **8**, 16117 (2017).
16. Gopalakrishnan, S. & Vasseur, R. Kinetic theory of spin diffusion and superdiffusion in *XXZ* spin chains. *Phys. Rev. Lett.* **122**, 127202 (2019).
17. Ilievski, E., De Nardis, J., Medenjak, M. & Prosen, T. Superdiffusion in one-dimensional quantum lattice models. *Phys. Rev. Lett.* **121**, 230602 (2018).
18. Else, D. V., Monroe, C., Nayak, C. & Yao, N. Y. Discrete time crystals. *Annu. Rev. Condens. Matter Phys.* **11**, 467–499 (2020).
19. Basov, D. N., Averitt, R. D. & Hsieh, D. Towards properties on demand in quantum materials. *Nat. Mater.* **16**, 1077–1088 (2017).
20. Langen, T., Gasenzer, T. & Schmiedmayer, J. Prethermalization and universal dynamics in near-integrable quantum systems. *J. Stat. Mech.* **2016**, 064009 (2016).
21. Zhang, J. et al. Observation of a many-body dynamical phase transition with a 53-qubit quantum simulator. *Nature* **551**, 601–604 (2017).
22. Bernien, H. et al. Probing many-body dynamics on a 51-atom quantum simulator. *Nature* **551**, 579–584 (2017).
23. Barends, R. et al. Digital quantum simulation of fermionic models with a superconducting circuit. *Nat. Commun.* **6**, 7654 (2015).
24. Davis, E. J. et al. Protecting spin coherence in a tunable Heisenberg model. *Phys. Rev. Lett.* **125**, 060402 (2020).
25. Signoles, A. et al. Glassy dynamics in a disordered Heisenberg quantum spin system. Preprint at https://arxiv.org/abs/1909.11959 (2019).
26. Trotzky, S. et al. Time-resolved observation and control of superexchange interactions with ultracold atoms in optical lattices. *Science* **319**, 295–299 (2008).
27. Gross, C. & Bloch, I. Quantum simulations with ultracold atoms in optical lattices. *Science* **357**, 995–1001 (2017).
28. Jaksch, D., Bruder, C., Cirac, J. I., Gardiner, C. W. & Zoller, P. Cold bosonic atoms in optical lattices. *Phys. Rev. Lett.* **81**, 3108–3111 (1998).
29. Kuklov, A. B. & Svistunov, B. V. Counterflow superfluidity of two-species ultracold atoms in a commensurate optical lattice. *Phys. Rev. Lett.* **90**, 100401 (2003).
30. Duan, L.-M., Demler, E. & Lukin, M. D. Controlling spin exchange interactions of ultracold atoms in optical lattices. *Phys. Rev. Lett.* **91**, 090402 (2003).
31. García-Ripoll, J. J. & Cirac, J. I. Spin dynamics for bosons in an optical lattice. *New J. Phys.* **5**, 76 (2003).
32. Altman, E., Hofstetter, W., Demler, E. & Lukin, M. D. Phase diagram of two-component bosons on an optical lattice. *New J. Phys.* **5**, 113 (2003).
33. Amato-Grill, J., Jepsen, N., Dimitrova, I., Lunden, W. & Ketterle, W. Interaction spectroscopy of a two-component Mott insulator. *Phys. Rev. A* **99**, 033612 (2019).
34. Jordan, P. & Wigner, E. Über das Paulische Äquivalenzverbot. *Z. Phys.* **47**, 631–651 (1928).
35. Ioffe, A. F. & Regel, A. R. Non-crystalline, amorphous and liquid electronic semiconductors. *Prog. Semiconduct.* **4**, 237–291 (1960).
36. Mott, N. F. Conduction in non-crystalline systems IX. the minimum metallic conductivity. *Philos. Mag. A* **26**, 1015–1026 (1972).
37. Brown, P. T. et al. Bad metallic transport in a cold atom Fermi–Hubbard system. *Science* **363**, 379–382 (2019).
38. Dubkov, A. A., Spagnolo, B. & Uchaikin, V. V. Lévy flight superdiffusion: an introduction. *Int. J. Bifurc. Chaos* **18**, 2649–2672 (2008).
39. Andreev, A. È. et al. Correlation theory of processes with stationary random increments of order *n*. *Am. Math. Soc. Transl.* **8**, 87 (1958).
40. Agarwal, K., Gopalakrishnan, S., Knap, M., Müller, M. & Demler, E. Anomalous diffusion and Griffiths effects near the many-body localization transition. *Phys. Rev. Lett.* **114**, 160401 (2015).
41. Vosk, R., Huse, D. A. & Altman, E. Theory of the many-body localization transition in one-dimensional systems. *Phys. Rev. X* **5**, 031032 (2015).
42. Guardado-Sanchez, E. et al. Subdiffusion and heat transport in a tilted two-dimensional Fermi–Hubbard system. *Phys. Rev. X* **10**, 011042 (2020).
43. Antal, T., Rácz, Z., Rákos, A. & Schütz, G. M. Transport in the XX chain at zero temperature: emergence of flat magnetization profiles. *Phys. Rev. E* **59**, 4912–4918 (1999).
44. Gobert, D., Kollath, C., Schollwöck, U. & Schütz, G. Real-time dynamics in spin-$\frac{1}{2}$ chains with adaptive time-dependent density matrix renormalization group. *Phys. Rev. E* **71**, 036102 (2005).
45. Misguich, G., Pavloff, N. & Pasquier, V. Domain wall problem in the quantum XXZ chain and semiclassical behavior close to the isotropic point. *SciPost Phys.* **7**, 025 (2019).
46. Ljubotina, M., Žnidarič, M. & Prosen, T. A class of states supporting diffusive spin dynamics in the isotropic Heisenberg model. *J. Phys. A Math. Theor.* **50**, 475002 (2017).
47. Castro-Alvaredo, O. A., Doyon, B. & Yoshimura, T. Emergent hydrodynamics in integrable quantum systems out of equilibrium. *Phys. Rev. X* **6**, 041065 (2016).
48. Bertini, B., Collura, M., De Nardis, J. & Fagotti, M. Transport in out-of-equilibrium *XXZ* chains: exact profiles of charges and currents. *Phys. Rev. Lett.* **117**, 207201 (2016).
49. Caux, J.-S. & Mossel, J. Remarks on the notion of quantum integrability. *J. Stat. Mech.* **2011**, P02023 (2011).
50. Dimitrova, I. et al. Enhanced superexchange in a tilted Mott insulator. *Phys. Rev. Lett.* **124**, 043204 (2020).

Methods

Extended Hubbard model

To determine the parameters J_{xy} and J_z in equation (1)

$$J_{xy} = -\frac{4\tilde{t}^2}{U_{\uparrow\downarrow}}, J_z = \frac{4\tilde{t}^2}{U_{\uparrow\downarrow}} - \left(\frac{4\tilde{t}^2}{U_{\downarrow\downarrow}} + \frac{4\tilde{t}^2}{U_{\downarrow\downarrow}}\right)$$

we use measurements of the lattice depths V_x, V_y, V_z and of the three scattering lengths $a_{\uparrow\uparrow}$, $a_{\uparrow\downarrow}$, $a_{\downarrow\downarrow}$. From the calibrated lattice depths, the Hubbard parameters $\tilde{t}^{(0)}$ (in the non-interacting limit) and $U^{(0)}$ (in the single-band approximation) are calculated as[28]

$$\tilde{t}^{(0)} = -\int \mathrm{d}z w_z^*(z-a)\left[-\frac{\hbar^2}{2m}\frac{\mathrm{d}^2}{\mathrm{d}z^2} + V_z \sin^2(kz)\right] w_z(z),$$

and

$$U_{\sigma\sigma'}^{(0)} = g_{\sigma\sigma'}\int \mathrm{d}^3 r\, |w(\mathbf{r})|^4,$$

where $g_{\sigma\sigma'} = 4\pi\hbar^2 a_{\sigma\sigma'}/m$ and $\sigma, \sigma' = \uparrow, \downarrow$ and $w(\mathbf{r}) = w_x(x)\, w_y(y)\, w_z(z)$ using the calculated lowest-band Wannier functions $w_x(x)$, $w_y(y)$ and $w_z(z)$ for each lattice depth[51].

For the precision needed to compare experiment to theory, three corrections are applied[7,52–54].

Correction 1. Tunnelling is modified by the so-called single-band bond charge[54], which for single-occupancy is

$$\tilde{t}_{\sigma\sigma'} = \tilde{t}^{(0)} - g_{\sigma\sigma'}\int \mathrm{d}^3 r\, w^*(\mathbf{r}-\delta\mathbf{r}) w^*(\mathbf{r}) w(\mathbf{r}) w(\mathbf{r}),$$

where $\delta\mathbf{r} = (0, 0, a)$ is a displacement by one lattice constant a in the tunnelling direction. Through this correction, the tunnelling matrix elements $\tilde{t}_{\uparrow\uparrow}$, $\tilde{t}_{\uparrow\downarrow}$ and $\tilde{t}_{\downarrow\downarrow}$ are now slightly spin-dependent.

Correction 2. For the on-site interaction, we include admixtures of higher bands[53,54]. The dominant part is captured by a perturbative correction due to the first and second excited bands

$$U_{\sigma\sigma'} = U_{\sigma\sigma'}^{(0)} - g_{\sigma\sigma'}^2 \sum_{\mathbf{n}_1,\mathbf{n}_2} \frac{1}{E_{\mathrm{bg}}}\int \mathrm{d}^3 r\, w_{\mathbf{n}_1}^*(\mathbf{r}) w_{\mathbf{n}_2}^*(\mathbf{r}) w(\mathbf{r}) w(\mathbf{r}),$$

where $\mathbf{n}_1$ and $\mathbf{n}_2$ are the three-dimensional band indices of the two atoms and E_{bg} is the sum of the bandgap energies. Corrections to the tunnelling rate $\tilde{t}$ owing to population of higher bands is negligible for a Mott insulator with occupation $n = 1$, because higher bands are admixed only through virtual doubly occupied sites. These modifications of $\tilde{t}$ and U both contribute to a modification of superexchange J_{xy} and J_z (Extended Data Fig. 1). The relative correction to $J_{xy}^{(0)} = -4(\tilde{t}^{(0)})^2/U_{\uparrow\downarrow}^{(0)}$, given by $(J_{xy} - J_{xy}^{(0)})/J_{xy}^{(0)}$, is almost independent of lattice depth (for the range of lattice depths studied here), and in the experiment J_{xy} is typically reduced by 10% to 15%. Note that the correction has the opposite sign as in ref. [7], because $J_{xy} > 0$ is antiferromagnetic in the present work.

Correction 3. To accurately determine J_z, one must also consider off-site interactions of the form[54]

$$V_{\sigma\sigma'} = g_{\sigma\sigma'}\int \mathrm{d}^3 r\, w^*(\mathbf{r}-\delta\mathbf{r}) w^*(\mathbf{r}) w(\mathbf{r}-\delta\mathbf{r}) w(\mathbf{r}),$$

where $\delta\mathbf{r}$ is defined as before. One finds that J_z is modified by the addition of $2(V_{\uparrow\uparrow} + V_{\downarrow\downarrow} - 2V_{\uparrow\downarrow})$. Depending on the signs and magnitudes of the three interactions, the off-site terms can add to or subtract from the two previously discussed corrections to J_z (Extended Data Fig. 1).

Determination of the Heisenberg parameters

We calibrate the lattice depth using amplitude modulation spectroscopy[55]. We record the excitation spectrum of a Bose–Einstein condensate in a 1D lattice when the depth of the lattice is modulated by 3% providing the cloud-averaged lattice depth with a statistical uncertainty of 0.2%. Owing to an asymmetric excitation profile, we estimate a systematic error of 1%.

The lowest and second-lowest hyperfine states of ^{7}Li realize the $|\downarrow\rangle$ and $|\uparrow\rangle$ states. We use our previous measurements of $U_{\uparrow\uparrow}$ and $U_{\downarrow\downarrow}$ (lattice-depth modulation) as well as measurements of $U_{\uparrow\uparrow} - U_{\uparrow\downarrow}$ and $U_{\uparrow\downarrow} - U_{\downarrow\downarrow}$ (interaction spectroscopy)[33] to determine the three scattering lengths $a_{\uparrow\uparrow}$, $a_{\uparrow\downarrow}$ and $a_{\downarrow\downarrow}$ (under inclusion of higher-band corrections) for several magnetic fields B. The determined anisotropies Δ are shown in Fig. 1b (points). Hyperbolic fits to $a_{\uparrow\uparrow}(B)$, $a_{\uparrow\downarrow}(B)$ and $a_{\downarrow\downarrow}(B)$ are used to interpolate the values for the anisotropy (solid line). Extended Data Fig. 1 shows $a_{\uparrow\uparrow}$, $a_{\uparrow\downarrow}$ and $a_{\downarrow\downarrow}$, as well as J_{xy}, J_z and Δ with (and without) corrections. A recent detailed theoretical analysis[56] of the interaction spectroscopy data also provided precise scattering lengths across several Feshbach resonances. However, this analysis slightly disagreed with our lattice-depth modulation data in the range of magnetic fields studied here, and therefore we relied on the experimental data.

The Gaussian intensity profile of the lattice beams ($1/e^2$ radius of 125 μm) causes inhomogeneity of the lattice depth by up to 1.7% across a Mott insulator of 44 lattice sites in diameter. The 1.0% variation of U across the atom cloud can be neglected. The tunnelling coefficient $\tilde{t}$ within the spin chains is defined by the lattice depth V_z along the chains. Although it is constant within each spin chain, it varies among the chains by up to 4.4%, which increases superexchange J_{xy} by up to 9.0%. The curvature of the transverse lattice beams (with V_x, $V_y = 35E_R$) causes harmonic confinement $\frac{1}{2}m\omega_{\mathrm{trap}}^2 z^2 = \frac{1}{2}\kappa z^2$ along the chains with $\omega_{\mathrm{trap}} = 2\pi \times 770$ Hz or curvature $\kappa = h \times 116.6\ \mathrm{Hz}\, a^{-2}$, where h is the Planck constant. The curvature leads to a varying energy offset δ between neighbouring lattice sites, which is largest at the ends $z = \pm 22a$ of the longest spin chains. It modifies the energy of the intermediate state in the superexchange process $U \mapsto U \pm \delta$ (refs. [26,50]) and therefore increases the superexchange rate at the ends of the longest chains by 24% ($\Delta \approx 0$) and 11% ($\Delta \approx 1$), with an average value over all atoms of 4.2% ($\Delta \approx 0$) and 2.0% ($\Delta \approx 1$), respectively.

The lattice depth calibration and the experimental determination of the scattering length $a_{\uparrow\downarrow}$ lead to an uncertainty for the spin-exchange times $\hbar/J_{xy}$ of about ±10%. The accuracy of the determined anisotropies Δ is limited by the experimental determination of all scattering lengths $a_{\uparrow\uparrow}$, $a_{\uparrow\downarrow}$, $a_{\downarrow\downarrow}$. The uncertainty of Δ is estimated to be about ±0.1.

In the experiment (see Fig. 1b), $\Delta \approx 0$ was realized by tuning the magnetic field to $B_0 = 882.63$ G. Here the measured Hubbard parameters result in $\Delta = -0.12$ including higher-order corrections (and $\Delta = -0.02$ without corrections). We find that the spin dynamics in this regime is only weakly dependent on Δ, so we refer to measurements here as $\Delta \approx 0$. $B_0' = 842.95$ G is a second magnetic field value, which also realizes $\Delta \approx 0$ ($\Delta = -0.13$ including corrections and $\Delta = 0.01$ without corrections). We directly compare these two points B_0 and B_0' in Extended Data Fig. 5, and observe quantitative agreement. Arbitrary anisotropies were realized by using the magnetic field region in between: $B_0' < B < B_0$. In particular, for values $\Delta > 0$ ($\Delta < 0$) we used magnetic fields $B < 850$ G ($B > 850$ G). The isotropic point $\Delta \approx 1$ was realized at $B_1 = 847.30$ G (actually $\Delta = 1.01$ and corrections here are negligible).

In the following we give typical absolute values for Hubbard parameters at a lattice depth of $V_z = 11E_R$ and V_x, $V_y = 35E_R$. The recoil energy is $E_R/h = 25.12$ kHz.

XX model. $\Delta \approx 0$ is realized by the scattering lengths $a_{\uparrow\uparrow} = +307a_0$, $a_{\uparrow\downarrow} = -50a_0$ and $a_{\downarrow\downarrow} = -44a_0$, resulting in the following values for the on-site interactions $U_{\uparrow\uparrow}/h = +30.6$ kHz, $U_{\uparrow\downarrow}/h = -5.8$ kHz and $U_{\downarrow\downarrow}/h = -5.1$ kHz. The bare single-particle tunnelling coefficient is

given by $\tilde{t}^{(0)}/h = 380$ Hz, but interactions make tunnelling spin-dependent: $\tilde{t}_{\uparrow\uparrow}/h = 480$ Hz, $\tilde{t}_{\uparrow\downarrow}/h = 370$ Hz, and $\tilde{t}_{\downarrow\downarrow}/h = 370$ Hz. That results in the following Heisenberg parameters: $J_{xy}/h = 93.3$ Hz and $J_z/h = -10.9$ Hz.

XXX model. $\Delta \approx 1$ is realized by the scattering lengths $a_{\uparrow\uparrow} = -107a_0$, $a_{\uparrow\downarrow} = -71a_0$ and $a_{\downarrow\downarrow} = -53a_0$, resulting in $U_{\uparrow\uparrow}/h = -12.7$ kHz, $U_{\uparrow\downarrow}/h = -8.4$ kHz and $U_{\downarrow\downarrow}/h = -6.1$ kHz; and $\tilde{t}^{(0)}/h = 380$ Hz, $\tilde{t}_{\uparrow\uparrow}/h = 350$ Hz, $\tilde{t}_{\uparrow\downarrow}/h = 360$ Hz and $\tilde{t}_{\downarrow\downarrow}/h = 370$ Hz; and $J_{xy}/h = 62.6$ Hz and $J_z/h = 63.5$ Hz.

Superexchange coupling ($J_{xy}^{\perp}/h \approx 20$ mHz) between chains is negligible, owing to the deep transverse optical lattices (V_x, $V_y = 35E_R$) and is 3 to 4 orders of magnitude smaller than J_{xy}/h within the chains.

Experimental setup

In the experiment, we prepare 4.5×10^4 ^{7}Li atoms in an optical lattice with spacing $a = 532$ nm in the Mott insulating regime with one atom per site[50]. A Bose–Einstein condensate (with barely detectable thermal fraction $N_{th}/N \leq 0.05$) with all atoms in the $|\uparrow\rangle$ state is loaded into the optical lattice, with the scattering length set to strong repulsive interactions $a_{\uparrow\uparrow} = +307a_0$. This suppresses doubly occupied sites[50], which we counted directly by interaction spectroscopy[33] to be ≤0.5% of the total atom number. (Even a long spin chain of length $L = 44a$ has then only a probability ≤20% to contain a doubly occupied site.) The hole fraction is estimated to be between 5% and 10% through comparison of spin dynamics with theory (Fig. 2a). The density degree of freedom is frozen out after loading into the deep optical lattice, and the on-site interactions $U_{\uparrow\uparrow}$, $U_{\uparrow\downarrow}$ and $U_{\downarrow\downarrow}$ can then be varied freely without affecting the global atom distribution, as long as the atoms stay in the Mott insulating regime[50].

We then prepare a far-from-equilibrium initial spin state and probe the spin dynamics in one dimension. The lattice beams in the x and y directions are kept at a large constant depth of V_x, $V_y = 35E_R$ separating the atoms into an array of independent 1D chains, with a typical maximum length of $L_{max} = 44a$ (given by the diameter of the Mott insulator), and with an average length of $\langle L \rangle = 33a$ (Extended Data Fig. 10). The depth of $35E_R$ is sufficient to prevent superexchange coupling in the x and y directions ($\hbar/J_{xy}^{\perp} \approx 10$ s) on experimental timescales. Initially, the z-lattice depth is also $35E_R$. The magnetic field is then ramped to the value required for a desired anisotropy Δ. Using radio frequency pulses and a magnetic field gradient, a helical spin pattern is created where the spin component along the chain winds in the xz plane of the Bloch sphere with a wavevector $Q = 2\pi/\lambda$, where λ is the wavelength of the spin helix (see Fig. 1c and Methods section 'Preparation of the spin helix'). For λ smaller than the system size, the total magnetization of this state is close to zero.

The power of the lattice beam in the z direction controls the superexchange rate within the chains. Time evolution is initiated by ramping down the z-lattice depth V_z to a value between $9E_R$ and $13E_R$. The ramp time is 0.5 ms, fast compared to superexchange $\hbar/J_{xy}$, but slow compared to tunnelling $\hbar/\tilde{t}$. The ensuing coherent dynamics along each chain is governed by a 1D Heisenberg XXZ model with anisotropy Δ, equation (1). This is a quantum quench to a far-from-equilibrium initial state. After a variable evolution time t the dynamics is frozen by rapidly increasing the lattice depth back to $35E_R$. The atoms are then imaged in the $|\uparrow\rangle$ state via state-selective polarization-rotation imaging (see below).

Preparation of the spin helix

A global π/2 pulse of 75 μs rotates the spin $|\uparrow\rangle_i$ on each site i into the xy plane of the Bloch sphere $|\varphi\rangle_i = [|\uparrow\rangle_i + |\downarrow\rangle_i]/\sqrt{2}$. An applied magnetic field gradient in the z direction causes spin precession at rates that depend linearly on position z_i of the spin thus creating a spin helix $|\varphi\rangle_i = [|\uparrow\rangle_i + e^{-iQz_i}|\downarrow\rangle_i]/\sqrt{2}$ where the spin winds in the xy plane[7–9]. The strength and duration of the gradient determine the wavevector $Q = 2\pi/\lambda$ where λ is the wavelength of the spin helix. After turning off the gradient, an additional π/2 pulse rotates the spin helix into a state where the spin winding occurs in the xz plane $|\varphi\rangle_i = \cos(Qz_i/2)|\downarrow\rangle_i - \sin(Qz_i/2)|\uparrow\rangle_i$, so that the full many-body xz spin-helix state is $|\psi(Q)\rangle = \prod_i |\varphi\rangle_i$. In practice, the phase of the winding, θ, varies from realization to realization, which amounts to replacing $Qz_i \mapsto Qz_i + \theta$. This is caused by small magnetic bias field drifts on the 10^{-5} level. The range of λ used in the experiment was limited on the short side by optical resolution to $\lambda \geq 5.6a$ and on the long side by the length of the chains $L_{max} = 44a$.

When turning off the magnetic field gradient, special care was taken to cancel any residual gradients to better than $|B'| \leq 0.4$ mG cm^{-1}. The differential magnetic moment is typically $\Delta\mu/h = (\mu_\uparrow - \mu_\downarrow)/h \approx 30$ kHz G^{-1} (it varies by approximately 10% depending on the bias field B). This translates to a maximum energy difference of $\Delta\mu B' L_{max}/h = 0.3$ Hz across the chain length, completely negligible compared to the spin-exchange coupling J_{xy}/h, which is 2 to 3 orders of magnitude larger.

Imaging

The optical density of the atomic ensemble is too high (>14) to allow for in situ observation of the modulation of $\langle S^z \rangle$ via absorption imaging. Instead, we use dispersive imaging, which uses the phase accumulated by the transmitted light to form an image of the atomic density distribution. When light at frequency ω_L is detuned from the atomic resonance ω_0 by many natural linewidths Γ, it picks up an approximate phase $\theta \approx -2\Delta\omega/\Gamma \times \mathrm{OD}(y, x, \Delta\omega)$, where OD is the optical density at detuning $\Delta\omega = \omega_L - \omega_0$, while absorption is suppressed by a sufficiently large detuning $\Delta\omega$. To form an image, the phase-shifted light must be interfered with a reference beam. In this work, we make use of the fact that the optical transition we use for imaging is driven only by a single polarization component; after passing through the atoms, the shifted and unshifted components are combined on a polarizer. A judicious choice of input and output polarizers yields an interference signal I on the camera[57,58] that is $I = I_0(1 - \sin\theta)/2$.

The optical resolution of our imaging system (with a numerical aperture of NA ≈ 0.2) was determined to have a cut-off at modulation wavelength $\lambda \approx 3.0$ μm $= 5.6a$ (330 line pairs per mm). The reduction of the modulation transfer function MTF(Q) near the cut-off reduces the observed contrast $\mathcal{C}(t) = \mathrm{MTF}(Q)c(t)$ compared to the real contrast $c(t)$. This does not affect the decay times τ. Assuming that the experimental preparation sequence for the initial spin-helix state achieves full contrast $c(0) = 1$ for any wavevector Q (based on careful pulse calibration and characterization), we can use $\mathcal{C}(0)$ as a direct measurement of MTF(Q) and determine the real contrast as $c(t) = \mathcal{C}(t)/\mathcal{C}(0)$.

Constant background contrast

For long evolution times t, the contrast $c(t)$ does not fully decay, but reaches a background value c_0, for example $c_0 = 0.08(1)$ in Fig. 2a. The numerical simulations, however, show a decay to zero. Therefore we add here the fit value for c_0 to the simulations for better comparison with experimental results. The experimental offset is caused by the inhomogeneous density of the atom cloud: only 90% of the atoms are in the Mott insulator state, which realizes an array of 1D spin chains. A small fraction of atoms are in dilute spatial wings, separated by holes that are immobile, owing to the gradient of the trapping potential (which suppresses first-order tunnelling, as shown in our previous work)[50]. These atoms preserve an imprinted spin-modulation pattern for long times. We have checked this mechanism by increasing the amount of thermal atoms and clearly observe an increase of the background c_0 (Extended Data Fig. 4). Furthermore, a position-sensitive measurement of the contrast confirms that the main contribution is indeed from atoms in the spatial wings (Extended Data Fig. 4f–g). In agreement with this model, numerical simulations always show a decay to zero for long spin chains (see Extended Data Figs. 6, 7, 9, 10). Experiments throughout this Article were performed with the lowest thermal fraction $N_{th}/N \leq 0.05$, where the contrast decays (almost) uniformly across the whole atom cloud, and offsets are small, so that it was not necessary to restrict the fits to the central part of the cloud (see Extended Data Fig. 2).

Time-reversal invariance of spin dynamics

For an *xz* spin-helix initial state and time evolution via the XXZ Hamiltonian, the contrast is time-reversal symmetric: $c(t) = c(-t)$, which follows because the state, Hamiltonian and observable (the local magnetization S_i^z) can be all expressed as real. This also implies invariance against the overall sign of the Hamiltonian $H \mapsto -H$. The same argument holds for the system with holes evolving under the bosonic $\tilde{t}$–J model. The initial dynamics of the contrast (in the ideal scenario) in both cases is therefore quadratic, $c(t) = 1 + \Gamma^2 t^2 + \ldots$, with

$$\Gamma^2 = -\frac{1}{\hbar^2}\frac{2a}{L}\sum_i \cos(Qz_i + \theta)\langle\psi(Q)|[H,[H,S_i^z]]|\psi(Q)\rangle.$$

Therefore the timescale of the initial quadratic decay $|\Gamma|^{-1}$ is the superexchange timescale $\hbar/J_{xy}$ (XXZ model) or the tunnelling timescale $\hbar/\tilde{t}$ ($\tilde{t}$–J model). The fact that, experimentally, we do not observe an initial quadratic behaviour indicates either (i) the presence of holes, but that we are not resolving the fast timescale $\hbar/\tilde{t}$; or (ii) that the initial state is not time-reversal invariant (that is, cannot be expressed as real, in the same basis that the Hamiltonian is written in). The latter could arise from pulse imperfections, or the fact that the ramp-down of the optical lattice takes place over a finite duration of time, leading to deviations from the ideal initial state. Nevertheless, we expect that the overall behaviour of the decay of the contrast—for example, the scaling behaviour of dynamics with wavevector Q—is not strongly affected by (i) or (ii).

Power-law scalings in the continuum limit

In the experiments we measured the exponents α of the power laws $\tau \propto Q^{-\alpha}$ in the short-wavelength regime $Q = 2\pi/(30a)$ to $2\pi/(6a)$ (Fig. 3). Now we investigate how the exponents depend on the range of wavevectors Q, in particular in the continuum limit $Q \to 0$ (where the wavelength λ of the modulation becomes large compared to the lattice spacing a and the discreteness of the underlying lattice is no longer relevant).

The short-time ($t \ll \hbar/J_{xy}$) Taylor expansion of the contrast $c(t) = 1 + \Gamma^2 t^2 + \ldots$ enables us to define a 'time constant' $\tau = |\Gamma|^{-1}$, which we can compute analytically even in the thermodynamic limit $L/a \to \infty$. This is because the object $\langle\psi(Q)|[H,[H,S_i^z]]|\psi(Q)\rangle$ is a strictly local quantity as the spin-helix state $|\psi(Q)\rangle$ is a product state and the commutator of the Hamiltonian with the local term S_i^z only produces terms near site i. Evaluating (with $\theta = 0$ for simplicity), we obtain

$$\Gamma^2 = \frac{J_{xy}}{\hbar^2}\frac{1}{16}[7 - \Delta - 8\cos(Qa) + 2\cos(2Qa) + (\Delta - 1)\cos(3Qa)].$$

The limiting behaviour of τ as $Q \to 0$ is therefore $\tau \approx (Q^2a^2/4)^{-1}\hbar/J_{xy}$ for $\Delta = 1$ and $\tau \approx [(3\sqrt{2}/8)Qa\sqrt{1-\Delta}]^{-1}\hbar/J_{xy}$ for $\Delta < 1$.

This implies a sharp crossover from ballistic scaling to diffusive scaling as Δ approaches 1 from below in the regime of small enough wavevectors, as shown in Extended Data Fig. 8d, e. In the same figure, we show the exponents determined for a range of finite wavevectors ($Q = 2\pi/(20a)$ to $2\pi/(6a)$) as used in experiments and numerics, and find a smooth crossover from a superdiffusive regime to diffusive regime, in agreement with numerical simulations in Fig. 3.

Although this short-time analysis for $t \ll \hbar/J_{xy}$ predicts the scalings seen in the numerical simulations, it is not clear how much of this analysis is applicable to the intermediate to long times t at which the experiments were performed. It also remains an open question as to why numerics predict a superballistic exponent $\alpha < 1$ for the XX model ($\Delta = 0$), but the experiment measures a ballistic exponent $\alpha \approx 1$. The discrepancy is possibly caused by the presence of holes, as suggested by the $\tilde{t}$–J model simulation (Fig. 3c).

Numerical simulations

In the numerical simulations we consider: (i) a spin-helix quench under XXZ Hamiltonian (equation (1)) dynamics, and (ii) a spin helix with 5% to 10% hole probability evolving under the bosonic $\tilde{t}$–J model (that is, assuming no doubly occupied sites), given by

$$H = \sum_{\langle ij\rangle}\left[J_{xy}(S_i^xS_j^x + S_i^yS_j^y) + J_zS_i^zS_j^z\right] + H_\mathrm{d},$$

$$H_\mathrm{d} = -\sum_{\sigma,\langle ij\rangle}\tilde{t}\,a_{\sigma i}^\dagger a_{\sigma j} - \sum_{\sigma,\langle ijk\rangle}\left[\frac{\tilde{t}^2}{U_{\uparrow\downarrow}}a_{\sigma i}^\dagger n_{\bar{\sigma}j}a_{\sigma k} + \frac{\tilde{t}^2}{U_{\uparrow\downarrow}}a_{\bar{\sigma}i}^\dagger S_j^\sigma a_{\sigma k} + \frac{2\tilde{t}^2}{U_{\sigma\sigma}}a_{\sigma i}^\dagger n_{\sigma j}a_{\sigma k}\right] + \mathrm{h.c.},$$

where spin $\sigma = \uparrow, \downarrow$. Here $a_{\sigma i}$ and $a_{\sigma i}^\dagger$ are bosonic lowering and raising operators at site i, respectively, $S_i^\uparrow \equiv S_i^+$ is defined as $a_{\uparrow i}^\dagger a_{\downarrow i}$, and $S_i^\downarrow \equiv S_i^-$ is defined as $a_{\downarrow i}^\dagger a_{\uparrow i}$. We use parameters from experiments and focus on a lattice depth of $11E_\mathrm{R}$, in which case we have $U_{\uparrow\downarrow}/U_{\uparrow\uparrow} = 1.206$, 1.406, 1.401, 1.398, 1.397 and 1.392, $U_{\uparrow\downarrow}/U_{\downarrow\downarrow} = -0.188$, 0.264, 0.459, 0.575, 0.659 and 0.862, and $U_{\uparrow\downarrow}/\tilde{t} = -17.94$, −24.32, −24.17, −24.08, −24.05 and −23.94 for anisotropies $\Delta = 0.020$, 0.670, 0.860, 0.973, 1.055 and 1.256, respectively. In the absence of holes, the action of the term H_d vanishes, and the Hamiltonian reduces to the XXZ Hamiltonian.

In both cases we use the real-time time-evolving block decimation (TEBD) method with matrix product states (MPS) on a spin chain with open boundary conditions. In case (i): local Hilbert space dimension = 2, length $L = 40a$ and bond dimensions up to 800; case (ii): local Hilbert space dimension = 3, $L = 40a$ for $\Delta = 0$, or $L = 20a$ for all other Δ. Simulations are cut-off in simulated time, owing to the rapid increase in entanglement of the state, requiring ever-increasing computational times. For the special case $\Delta = 0$, without holes, we alternatively use free fermionic methods, considerably speeding up the calculations. For technical reasons, instead of simulating the full distribution of holes we simply average over the situations in which there are either exactly one or two (or four) holes in the chain. For $L = 20a$ ($40a$), a single hole corresponds to an average of 5% (2.5%) holes.

To obtain the contrast, we determine the local magnetization $\langle S_i^z(t)\rangle = [\langle n_{i\uparrow}(t)\rangle - \langle n_{i\downarrow}(t)\rangle]/2$ and determine the Fourier component at wavevector Q via $c(t) = \frac{4a}{L}\sum_i \langle S_i^z(t)\rangle\cos(Qz_i + \theta)$, assuming that the initial spin helix has wavevector Q with a given phase θ (see Methods section 'Creation of the spin helix'); we then compare this to the experimental contrast. However, as noted in Methods section 'Time-reversal invariance of spin dynamics', the numerically simulated contrast always has an initial quadratic decay, unlike that seen in the experiments. We therefore determine the decay timescales and its power-law scaling with Q using one of the following methods. For positive anisotropies $\Delta \geq 0$, we define the decay time constant as the time it takes for the contrast $c(t)$ to decay from 1 to 0.6, divided by $-\ln(0.6)$ to convert to a '1/e' time (see Extended Data Fig. 6). For negative anisotropies $\Delta < 0$, for regime I we take the time to decay from 1 to 0.9, multiplied by 10 to extrapolate to zero, whereas for regime II we fitted a simple exponential-decay profile to obtain the decay timescales once the curves start 'peeling off' when plotted with time units rescaled by λ (see Fig. 4c and Extended Data Fig. 7). The resulting power-law scalings (Extended Data Fig. 8) and resulting exponents (Fig. 3c) are in reasonable agreement with the experimental results.

Finite-size effects

Numerical simulations can study the effect of different chain lengths L and initial phases θ of the spin helix on the dynamics. This is relevant because in the experiment, the atoms are distributed uniformly over a sphere with a typical diameter of $L_\mathrm{max} = 44a$ in three dimensions, leading to an ensemble of 1D chains of varying lengths. The experimentally measured contrast $c(t)$ is an average over all chain lengths with a probability distribution shown in Extended Data Fig. 10. Furthermore, owing to drifts of the applied magnetic field, the initial phase θ of the spin-helix state varies from shot to shot. Here we study numerically both effects.

We concentrate on the XX model ($\Delta = 0$) without holes. Extended Data Fig. 9 shows that the strong dependence of the contrast $c(t)$ on the initial phase θ is due to reflection of magnetization off the boundaries of the chain. This suggests that averaging over various chain lengths or averaging over initial phases should give similar results, which is confirmed in Extended Data Fig. 10. It is even sufficient to average over only two phases, $\theta = 0$ and $\pi/2$, to achieve insensitivity to initial and boundary conditions. The distribution of chains, and the simulation of a magnetization profile averaged over this distribution of chains, are illustrated in Extended Data Fig. 10b–d.

The conclusion is that the experiment is naturally performing an average over different phases and different chain lengths, washing out the sensitive dependence of the spin dynamics on initial conditions. For comparison with simulations, it is sufficient to use a system with a fixed chain length $L = 40a$, and average over only the two phases $\theta = 0$ and $\pi/2$.

Data availability

The data that support the findings of this study are available from the corresponding author upon reasonable request.

51. Greiner, M. *Ultracold Quantum Gases in Three-dimensional Optical Lattice Potentials*. PhD thesis, Ludwig-Maximilians-Universität München (2003).
52. Łącki, M., Delande, D. & Zakrzewski, J. Dynamics of cold bosons in optical lattices: effects of higher Bloch bands. *New J. Phys.* **15**, 013062 (2013).
53. Will, S. et al. Time-resolved observation of coherent multi-body interactions in quantum phase revivals. *Nature* **465**, 197–201 (2010).
54. Lühmann, D.-S., Jürgensen, O. & Sengstock, K. Multi-orbital and density-induced tunneling of bosons in optical lattices. *New J. Phys.* **14**, 033021 (2012).
55. Stöferle, T., Moritz, H., Schori, C., Köhl, M. & Esslinger, T. Transition from a strongly interacting 1D superfluid to a Mott insulator. *Phys. Rev. Lett.* **92**, 130403 (2004).
56. Secker, T., Amato-Grill, J., Ketterle, W. & Kokkelmans, S. High-precision analysis of Feshbach resonances in a Mott insulator. *Phys. Rev. A* **101**, 042703 (2020).
57. Bradley, C. C., Sackett, C. A. & Hulet, R. G. Bose–Einstein condensation of lithium: observation of limited condensate number. *Phys. Rev. Lett.* **78**, 985–989 (1997).
58. Ketterle, W., Durfee, D. S. & Stamper-Kurn, D. M. Making, probing and understanding Bose–Einstein condensates. In *Bose–Einstein Condensation in Atomic Gases* (eds Inguscio, M. et al.) 67–176 (IOS Press, 1999).

Acknowledgements We thank M. D. Lukin, N. Y. Yao and M. Knap for discussions, Y. K. Lee for experimental assistance, as well as C. M. E. Paus for sharing computing resources, and J. de Hond for comments on the manuscript. We acknowledge support from the NSF through the Center for Ultracold Atoms and grant number 1506369, NSF (grant number OAC-193471), ARO-MURI Non-Equilibrium Many-Body Dynamics (grant number W911NF-14-1-0003), AFOSR-MURI Photonic Quantum Matter (grant number FA9550-16-1-0323), AFOSR-MURI Quantum Phases of Matter (grant number FA9550-14-1-0035), ONR (grant number N00014-17-1-2253), ARO (grant number W911NF-20-1-0163), the Vannevar Bush Faculty Fellowship, and the Gordon and Betty Moore Foundation EPiQS Initiative (grant number GBMF4306).

Author contributions P.N.J., J.A.-G., I.D. and W.K. conceived the experiment. P.N.J., J.A.-G. and I.D. developed the experimental setup and took the data. P.N.J. led the data analysis. W.W.H. and E.D. developed the theoretical analysis. W.W.H. performed the numerical simulations. All authors discussed the results and contributed to the writing of the manuscript.

Competing interests The authors declare no competing interests.

Additional information
Correspondence and requests for materials should be addressed to P.N.J.
Peer review information *Nature* thanks Jean-Philippe Brantut, Tomaž Prosen and the other, anonymous, reviewer(s) for their contribution to the peer review of this work.
Reprints and permissions information is available at http://www.nature.com/reprints.

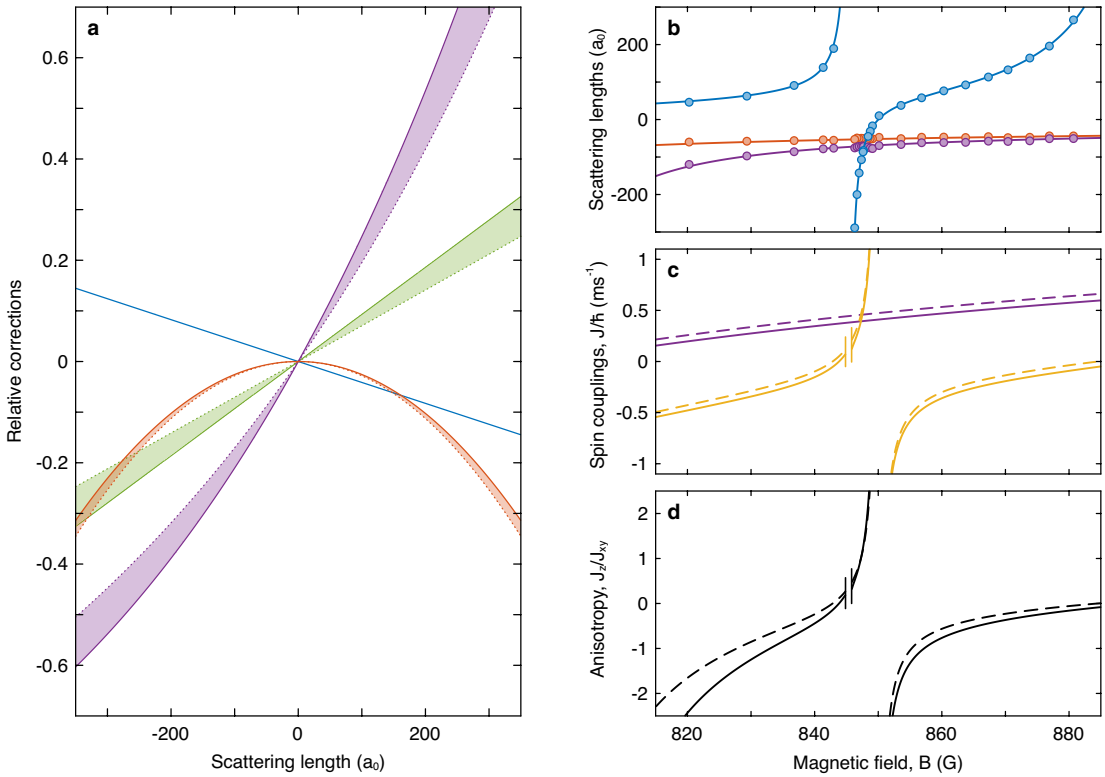

Extended Data Fig. 1 | Determination of the Heisenberg parameters. **a**, Corrections for tunnelling $(\tilde{t}-\tilde{t}^{(0)})/\tilde{t}^{(0)}$ (green), on-site interactions $(U-U^{(0)})/U^{(0)}$ (blue), superexchange $(J-J^{(0)})/J^{(0)}$ (purple) and off-site interactions $-2V/J^{(0)}$ (orange), where $\tilde{t}^{(0)}$, $U^{(0)}$ and $J^{(0)}=4(\tilde{t}^{(0)})^2/U^{(0)}$ are the uncorrected values and $\tilde{t}$, U and $J=4\tilde{t}^2/U$ include corrections, at a lattice depth of $13E_R$ (solid line) and $9E_R$ (dotted line). **b**, As a function of magnetic field B we show the scattering lengths $a_{\uparrow\uparrow}$ (blue), $a_{\uparrow\downarrow}$ (purple) and $a_{\downarrow\downarrow}$ (orange) measured in our previous work (points)[33]. Here a_0 is the Bohr radius. **c**, **d**, We interpolate the data in **b** using hyperbolic fits (solid lines) and calculate values for the transverse coupling constant J_{xy} (purple), the longitudinal coupling constant J_z (yellow) and the anisotropy $\Delta=J_z/J_{xy}$ (black), without corrections (dashed line) and including corrections (solid line) for a lattice depth of $11E_R$. The excluded region ($|a_{\uparrow\uparrow}|>700a_0$) is around a Feshbach resonance in the $|\uparrow\rangle$ state near 845.4 G.

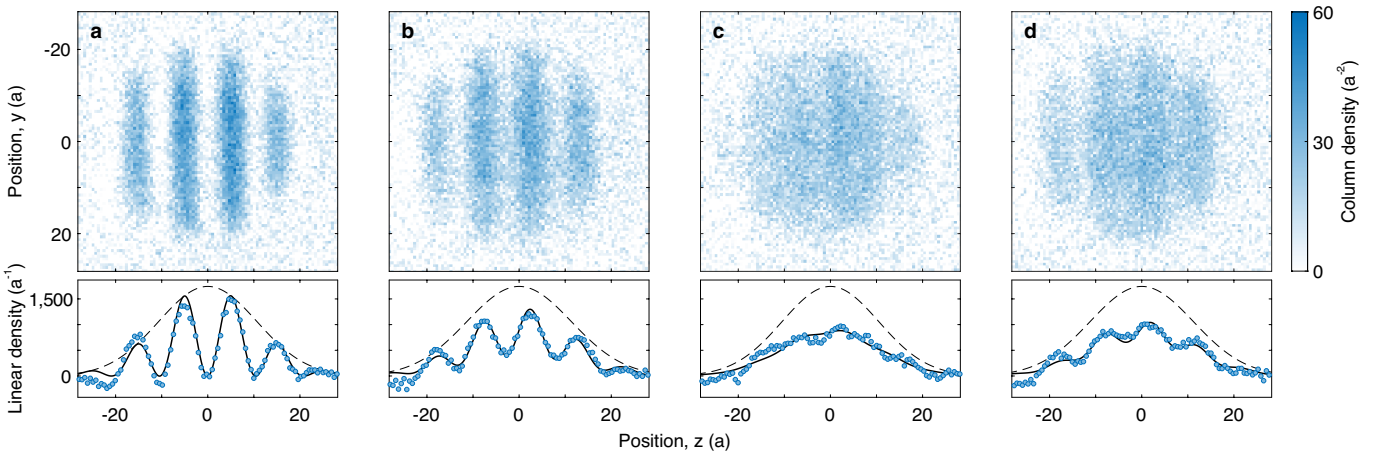

Extended Data Fig. 2 | Contrast measurement. a–**d**, The distribution of atoms in the $|\uparrow\rangle$ state. Every pixel is a local measurement of the column density (number of atoms per unit area). The y and z axes are displayed in units of the lattice spacing $a = 0.532\,\mu m$. The images are projected (integrated) along the y direction from $y = -30a$ to $+30a$ to obtain the linear density (number of atoms per unit length). The resulting 1D distributions are fitted with $f(z) = g(z)[1 + \mathcal{C}\cos(Qz + \theta)]/2$ (solid line), where $g(z)$ is a Gaussian envelope (dashed line), between $z = \pm 54a$. The data in **a**–**d** were measured at different evolution times $t = 0$ (**a**), $2.3\hbar/J_{xy}$ (**b**), $6.3\hbar/J_{xy}$ (**c**) and $12.0\hbar/J_{xy}$ (**d**), for anisotropy $\Delta \approx 0$ and wavelength $\lambda = 10.4a$. The obtained contrast $\mathcal{C}(t)$ is shown in Fig. 2a. In general, we also normalize by the initial contrast $\mathcal{C}(0)$ to correct for finite optical imaging resolution. This is important for shorter wavelengths λ close to the optical resolution of 3 µm, where the measured contrast $\mathcal{C}(t)$ is reduced compared to the real contrast $c(t) = \mathcal{C}(t)/\mathcal{C}(0)$.

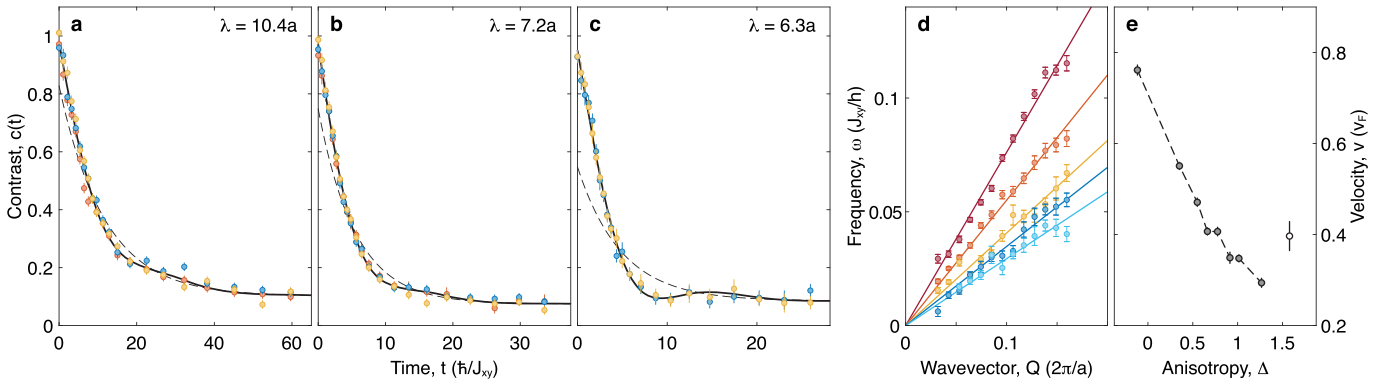

Extended Data Fig. 3 | Dispersion relations. For all positive anisotropies $\Delta \geq 0$, the time evolution of the contrast $c(t)$ shows a damped oscillatory component, in addition to the overall exponential decay. For larger Δ, the oscillations become smaller. **a**–**c**, Decay and weak oscillation at the isotropic point $\Delta \approx 1$ measured for different wavelengths λ, at three different lattice depths $9E_R$ (orange), $11E_R$ (blue) and $13E_R$ (yellow). Solid lines are fits $c(t) = [a_0 + b_0\cos(\omega t)]e^{-t/\tau} + c_0$ and dashed lines show the overall decay $a_0 e^{-t/\tau} + c_0$, around which the oscillations take place. The oscillations become more pronounced for short wavelengths λ, because the decay time ($\tau \propto \lambda^2$) decreases with smaller wavelength more strongly than the oscillation period ($T \propto \lambda$). **d**, The oscillation frequencies follow linear dispersion relations $\omega(Q) = vQ$ shown for $\Delta = -0.12$ (red), 0.35 (orange), 0.78 (yellow), 1.01 (blue) and 1.27 (light blue). **e**, The obtained velocities v decrease with increasing anisotropy Δ. For $\Delta = 1.58$ (open symbol), oscillations are small and the measurement was limited to large values of Q, which precluded recording a full dispersion relation. We note that although the oscillations are difficult to discern by eye (for example, in **a**), especially for large anisotropies Δ and small wavevectors Q, the fitted oscillation frequencies ω all fall very well on linear dispersion relations, which demonstrates that those barely visible oscillations are real. The linear scaling $\omega(Q) = vQ$ persists even in the superdiffusive, diffusive and subdiffusive regimes, where the power-law scaling of the decay time constant $\tau \propto Q^{-\alpha}$ is strongly nonlinear. This small ballistic (oscillatory) component may be related to our initial condition of a spin helix, which in the mapping to lattice fermions is a 100% density modulation, which reduces scattering at early times.

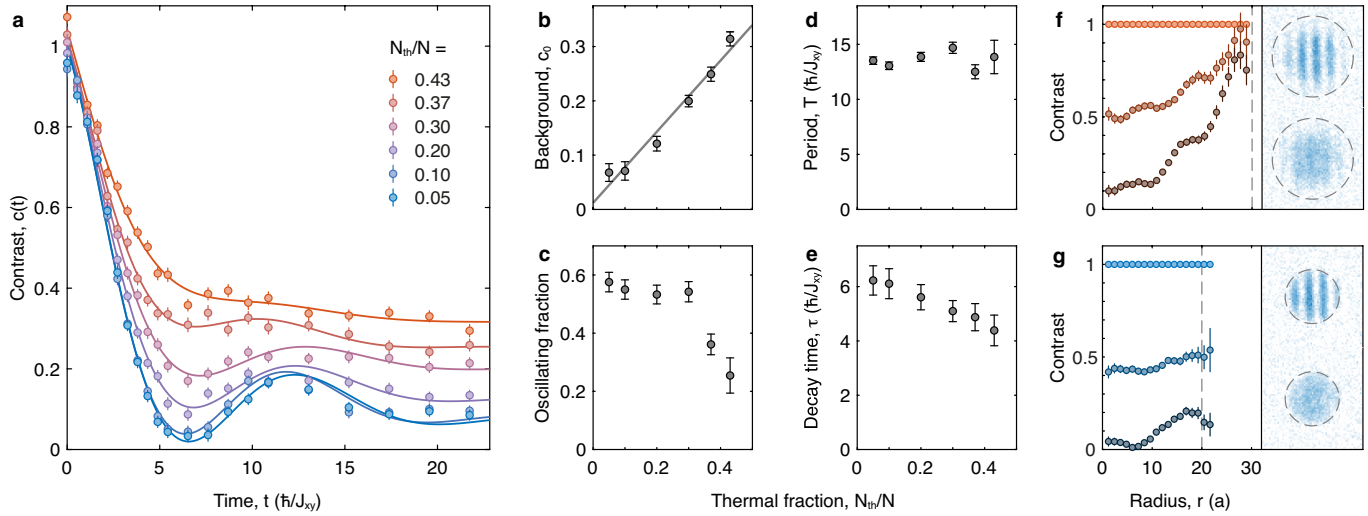

Extended Data Fig. 4 | Effect of finite hole concentration. By varying the thermal fraction N_{th}/N of the Bose–Einstein condensate before it is loaded into the optical lattice, we vary the energy and entropy of the atoms in the spin chain, and therefore the concentration of holes. (For our conditions, doubly occupied sites have higher energies than holes). Measurements are shown here for $\Delta \approx 0$ and $\lambda = 10.4a$, at a lattice depth of $11E_R$. **a**, Decay curves $c(t)$ for varying hole concentrations ranging from low (blue) to high (orange) thermal fraction. Solid lines are fits $c(t) = [a_0 + b_0\cos(\omega t)]e^{-t/\tau} + c_0$. **b**, The background contrast c_0 increases monotonously with thermal fraction N_{th}/N. A linear fit (solid line) extrapolates to $c_0 = 0.01(2)$, consistent with zero, for $N_{th}/N = 0$. This suggests that all of the background contrast is due to hole excitations. **c**, Higher hole concentrations suppress the oscillating fraction $b_0/(a_0 + b_0)$. **d**, Holes do not affect the oscillation period $T = 2\pi/\omega$. **e**, Holes decrease the decay time τ, albeit slightly. **b**–**e** show that almost all of our measurements are not sensitive to a small thermal fraction, which is usually $N_{th}/N \leq 0.05$ throughout this work. The behaviour shown in **c** and **e** is most probably caused by mobile holes in the central part of the Mott insulator. Indeed, numerical simulations of the $\tilde{t}$–J model reproduce such effects (Fig. 2a). Note though that for the isotropic case $\Delta \approx 1$, a previous work[7] found a ~50% change in decay time when the hole concentration changed from 0 to 5%. Our numerical simulations (Extended Data Fig. 8b) do not show such strong sensitivity (for any anisotropy, even at $\Delta = 1$), possibly owing to asymmetry in the on-site interactions ($U_{\uparrow\uparrow} \neq U_{\uparrow\downarrow} \neq U_{\downarrow\downarrow}$) in our system. On the other hand, a finite background contrast (**b**) is probably caused by immobile holes located in the outer parts of the atom distribution where first-order tunnelling is suppressed by the gradient of the (harmonic) trapping potential[50]. Immobile holes disrupt spin transport, and so we expect that the imprinted spin modulation in these regions will not (or only very slowly) decay. **f**, **g**, The region with immobile holes is visible as a shell of low atomic density surrounding the Mott insulator in the in situ images for large hole concentration (**f**) and is absent for low hole concentration (**g**). The three curves in both **f** and **g** show the local contrast as a function of distance r from the centre of the atom cloud for the evolution times $t = 0$ (top), $2.7\hbar/J_{xy}$ (middle) and $21.7\hbar/J_{xy}$ (bottom). The two in situ images in both **f** and **g** are for $t = 0$ (top) and $21.7\hbar/J_x$ (bottom). The dashed lines indicate contours of constant radius, $r = 30a$ (**f**) and $r = 20a$ (**g**).

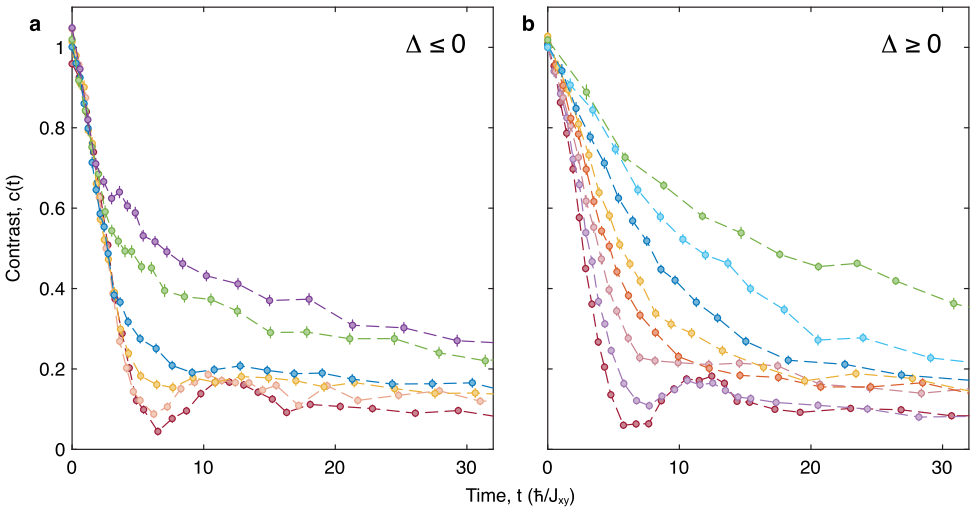

Extended Data Fig. 5 | Decay behaviour as a function of anisotropy. **a**, **b**, Decay behaviour ranging from negative (**a**) to positive (**b**) anisotropy, for a fixed wavelength $\lambda = 10.4a$. Using $\Delta \approx 0$ as a reference point, we show how the temporal profile of the decay curve $c(t)$ changes when we introduce positive or negative interactions. Every data point is an average of two measurements at lattice depths $11E_R$ and $13E_R$. In **a**, from bottom to top: $\Delta = -0.12$ (red), −0.59 (pink), −0.81 (yellow), −1.02 (blue), −1.43 (green) and −1.79 (purple). In **b**, from bottom to top: $\Delta = -0.13$ (red), 0.08 (purple), 0.35 (pink), 0.55 (orange), 0.78 (yellow), 1.01 (blue), 1.27 (light blue) and 1.58 (green). Regardless of sign, for increasing $|\Delta|$ the decay always slows down and the revivals damp more quickly. However, there is a big difference in how this slowdown happens: for increasing positive interactions $\Delta > 0$, the initial rate of decay decreases continuously (**b**); by contrast, for all negative interactions $\Delta < 0$, the initial rate of decay stays constant (and is ballistic), coinciding with the $\Delta \approx 0$ case (**a**). It is only after a critical time t_0 that the decay suddenly starts slowing down (and becomes diffusive) for times $t > t_0$. This critical time t_0 decreases with increasing negative interaction strength $|\Delta|$.

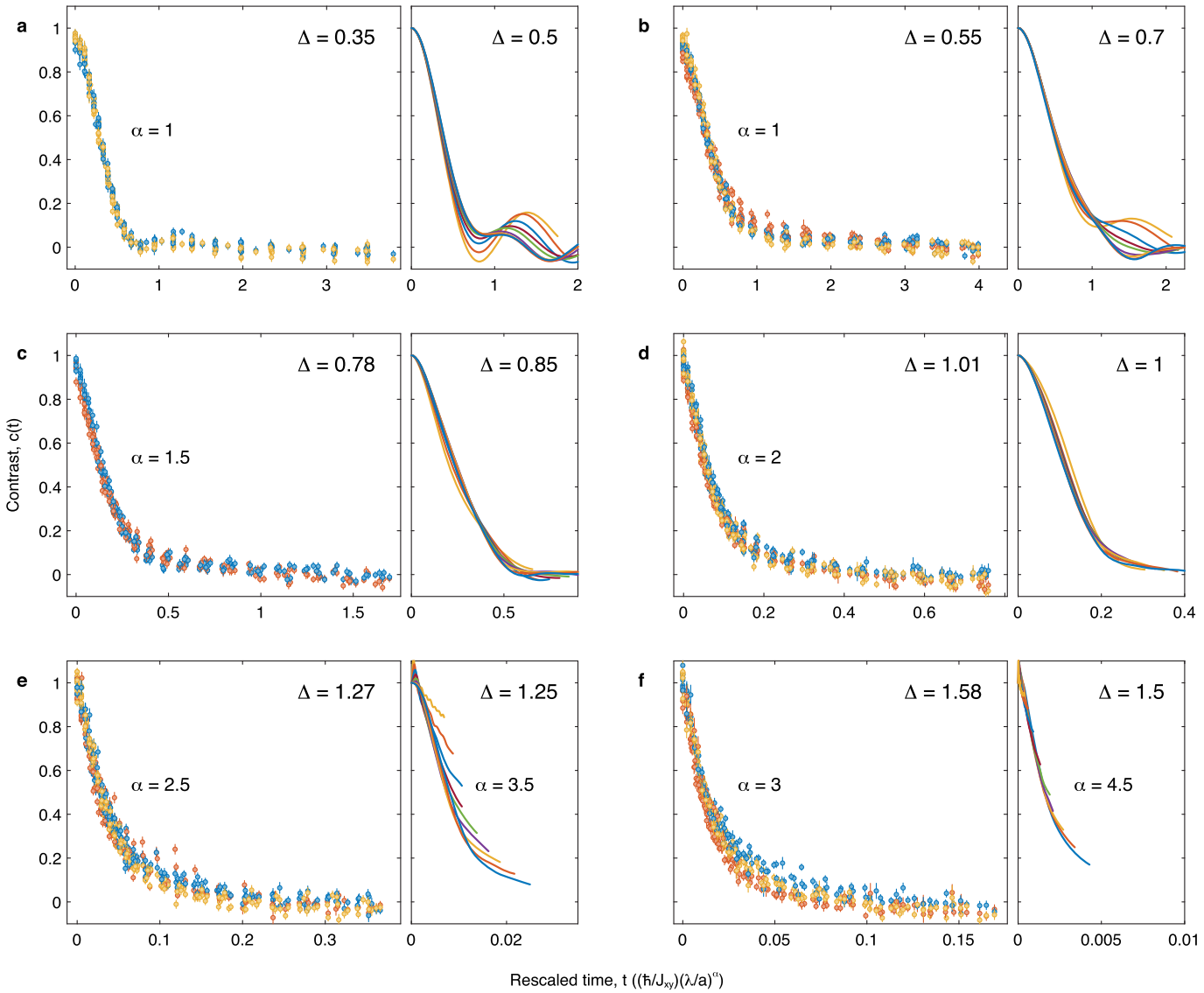

Extended Data Fig. 6 | Collapse of decay curves for positive anisotropies. All decay curves $c(t)$ for wavelengths $\lambda = 15.7a, 13.4a, 11.7a, 10.4a, 9.4a, 8.5a, 7.8a, 7.2a$ and $6.7a$ collapse very well into a single curve for all evolution times t, when time units are rescaled by λ^{α}, where the exponent α is a function of anisotropy Δ, both for experiment (points) and theory (solid lines). Experimental points were measured for lattice depths $9E_R$ (red), $11E_R$ (blue) and $13E_R$ (yellow). **a**, **b**, Ballistic regime ($\alpha = 1$). **c**, Superdiffusion ($\alpha = 1.5$). **d**, Diffusion ($\alpha = 2$). **e**, **f**, Subdiffusion ($\alpha = 2.5, 3$ for experiment and $\alpha = 3.5, 4.5$ for numerical simulations; in **f**, experiments covered a reduced range $\lambda \leq 10.4a$). For all anisotropies $\Delta \geq 0$ (**a**–**f**) the experimentally measured oscillation frequencies ω follow linear dispersion relations (Extended Data Fig. 3) and have a scaling behaviour different from the decay rates. However, such oscillations are small outside the ballistic regime $\alpha \approx 1$, and therefore only lead to a small deviation from the collapse behaviour. Note also the different timescales in experiments and simulations for $\Delta > 1$.

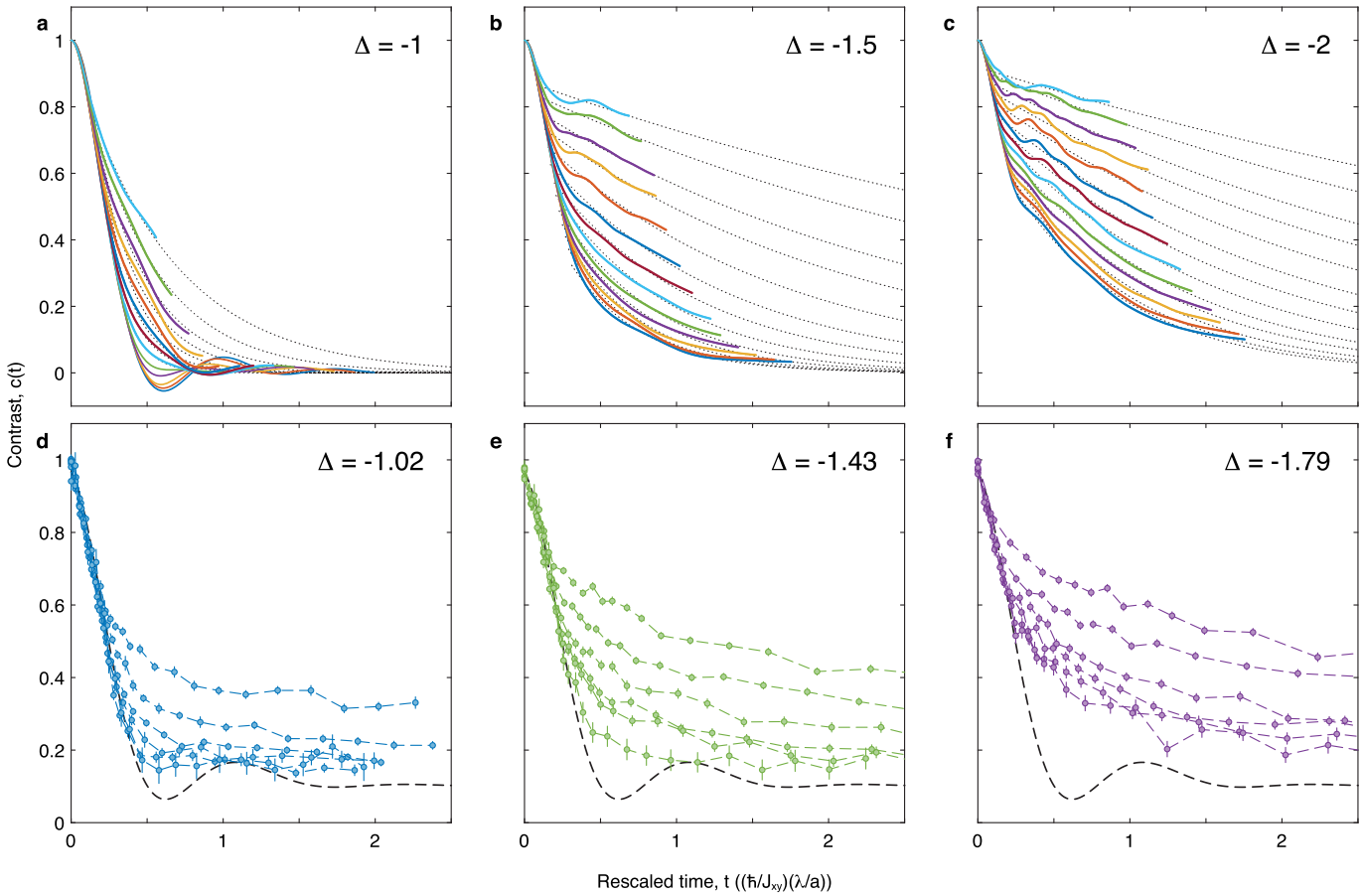

Extended Data Fig. 7 | Collapse at short times for negative anisotropies. All decay curves $c(t)$ for different wavelengths λ collapse into a single curve at early times, when time units are rescaled by λ (indicating ballistic behaviour). For later times the decay is diffusive with different scaling. **a**–**c**, Theory (from top to bottom: $\lambda = 31.3a, 23.5a, 18.8a, 15.7a, 13.4a, 11.7a, 10.4a, 9.4a, 8.5a, 7.8a, 7.2a, 6.7a$ and $6.3a$). The dotted lines are exponential fits $e^{-t/\tau_{II}}$ to the diffusive regime and the time constants τ_{II} are shown in Extended Data Fig. 8a. **d**–**f**, Experiment (from top to bottom: $\lambda = 18.8a, 13.4a, 10.4a, 8.5a, 7.2a$ and $6.3a$). Every data point is an average of two measurements at lattice depths $11E_R$ and $13E_R$. The black dashed line indicates the ballistic case $\Delta \approx 0$ (see Fig. 2c).

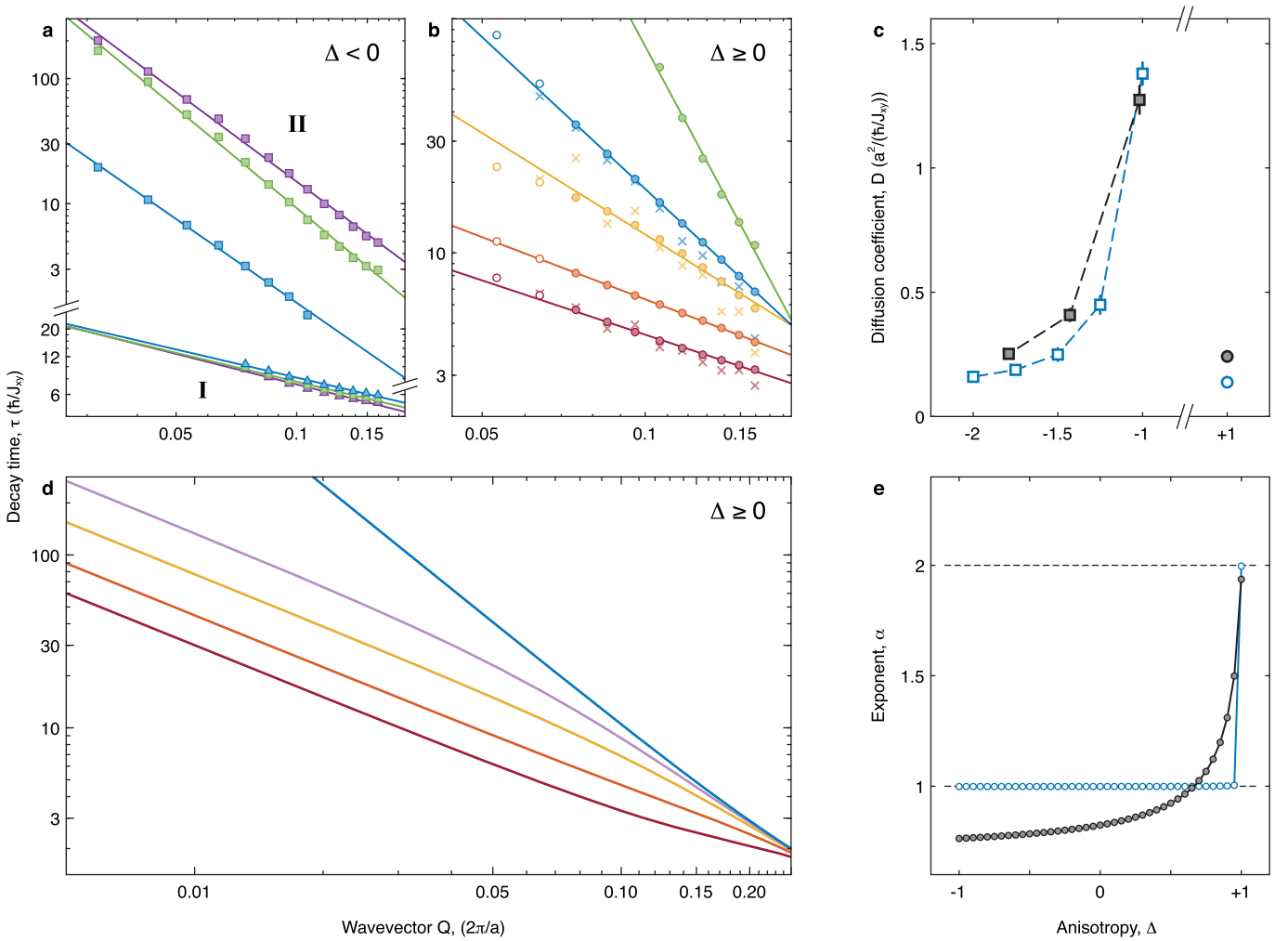

Extended Data Fig. 8 | Power-law scalings (theory) and diffusion coefficients. a, **b**, Decay time constants τ for different anisotropies Δ ranging from negative (**a**) to positive (**b**). Numerical results are shown in **a** for $\Delta = -1$ (blue), -1.5 (green) and -2 (purple) and in **b** for $\Delta = 0$ (red), 0.5 (orange), 0.85 (yellow), 1 (blue) and 1.5 (green). Solid lines are power-law fits (to the filled symbols). Open symbols are excluded from the fit owing to finite-size effects. Crossed symbols are results from $\tilde{t}$–J model simulations including 5% hole fraction. Fitted power-law exponents are shown in Fig. 3c. For positive anisotropies $\Delta \geq 0$ the decay time τ is defined as $\tau = \tau'/\ln(1/0.60)$ with $c(\tau') = 0.60$. For negative anisotropies $\Delta < 0$, the decay time τ_I for short times (I) is defined as $\tau_\mathrm{I} = 10\tau_\mathrm{I}'$ with $c(\tau_\mathrm{I}') = 0.90$. For longer times (II), the decay time τ_II is obtained from exponential fits e^{-t/τ_II} to the diffusive long-time tail (see dotted curves in Extended Data Fig. 7a–c). **c**, Diffusion coefficients for the diffusive long-time regime (II) obtained from theory (open symbols) and experiment (filled symbols). For negative anisotropies $\Delta < 0$, values were determined from quadratic power-law fits $1/\tau = DQ^2$ to the data points in **a** (theory) and Fig. 3a (experiment) for the diffusive regime (II). Note that for $\Delta \geq 0$ the system is only diffusive for $\Delta = +1$, as shown in **b** (theory) and Fig. 3b (experiment). From the experimental diffusion coefficients, we estimate mean free paths δx using the velocity $v = 0.76(1)v_\mathrm{F}$ from the ballistic short-time regime (I), and obtain $\delta x = 3.35(15)a$, $1.07(7)a$ and $0.66(4)a$ for $\Delta = -1.02$, -1.43 and -1.79, respectively. **d**, Short-time ($t \ll \hbar/J_{xy}$) decay constant $\tau = |\Gamma|^{-1}$ obtained from Taylor expansion of the contrast $c(t) = 1 + \Gamma^2 t^2 + \ldots$ as a function of Q, for $\Delta = 0$ (red), 0.55 (orange), 0.85 (yellow), 0.95 (purple) and 1 (blue). For $\Delta < 1$ all curves in the log–log plot asymptote to the same slope as $Q \to 0$ (continuum limit), whereas there are deviations for larger wavevectors Q. For $\Delta = 1$ the slope is instead different. This indicates that the power-law exponent α in $\tau \propto Q^{-\alpha}$ depends on the range of wavevectors Q used to determine it. **e**, Power-law exponents α determined for the short-wavelength regime between $\lambda = 6a$ and $20a$ (filled symbols) as in experiments and numerics, and for the long-wavelength regime between $\lambda = 150a$ and $200a$ (open symbols) approaching the continuum limit. In the former case, the exponents show a smooth crossover from superballistic to diffusive as $\Delta \to 1$ similar to that in the experiments and numerics, whereas in the latter case the exponents show a sharp jump from ballistic to diffusive occurring exactly at $\Delta = 1$.

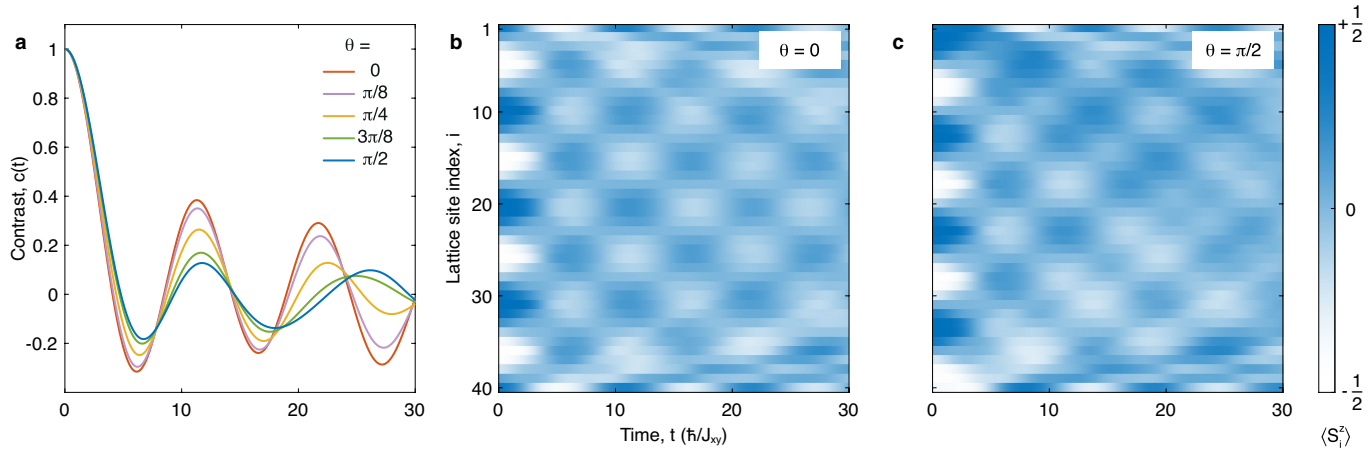

Extended Data Fig. 9 | Finite-size effects from the initial phase of the spin helix. a, The time evolution of the contrast $c(t)$ depends strongly on the initial phase θ, illustrated here by simulations for $\Delta = 0$ and $\lambda = 10.4a$. **b**, **c**, The dynamics of the local magnetization $\langle S_i^z(t)\rangle$ for phases $\theta = 0$ (**b**) and $\pi/2$ (**c**) reveals that this arises owing to the reflection of ballistically propagating magnetization off the ends of the chain. Depending on the initial phase of the spin helix, the reflected magnetization interferes constructively or destructively with the pattern of the bulk magnetization.

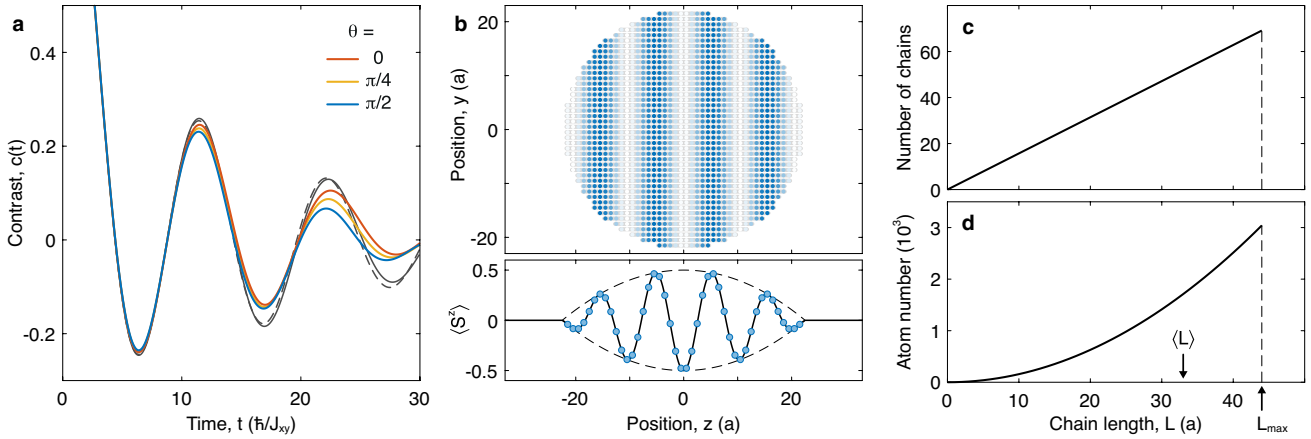

Extended Data Fig. 10 | Finite-size effects from the chain length. a, Contrast $c(t)$ obtained after a weighted average over all different chain lengths between $L = 0$ and $44a$ (shown in **b**), for $\Delta = 0$ and $\lambda = 10.4a$. The averaged dynamics (orange, yellow, blue) shows almost no dependence on the phase θ, in contrast to the dynamics determined from a single chain length $L = 40a$ (Extended Data Fig. 9a). Also overlaid are the contrasts for a fixed chain length ($L = 40a$) averaged over all initial phases $0 \le \theta < 2\pi$ (black solid line), and averaged over only the two phases $\theta = 0$ and $\pi/2$ (black dashed line). The close agreement implies that averaging over either chain lengths or phases suppresses the dependence on initial or boundary conditions. **b**, A cut through the spherical Mott insulator with diameter $L_{max} = 44a$ (as in the experiment) illustrates the distribution of different chain lengths (oriented along the z direction). Averaging the local magnetization S^z over the x and y directions provides a 1D magnetization profile (bottom panel), which is an average over all chains. **c**, The number of chains with length L is given by $(\pi/2)(L/a)$. The total number of chains is $\pi L_{max}/(2a)^2 \approx 1{,}500$. **d**, The number of atoms in chains with length L is given by $(\pi/2)(L/a)^2$. The contribution of each chain to the imaging signal is proportional to the atom number in the chain, and so the relevant average over chain lengths is weighted by the atom number and is $\langle L \rangle = (3/4)L_{max} = 33a$.